This is a preprint, the final version is subject to change, of the American Mineralogist (MSA)
Cite as Authors (Year) Title. American Mineralogist, in press.
(DOI will not work until issue is live.) DOI: http://dx.doi.org/10.2138/am.2014.4711

Ferroan Geikielite and Coupled Spinel-Rutile Exsolution from Titanohematite: Interface Characterization and Magnetic Properties

Robinson, Peter[1], Langenhorst, Falko[2*], McEnroe, S. A. [3], Fabian, Karl[1], and Boffa Ballaran, Tiziana[2]

[1] Geological Survey of Norway, N-7491 Trondheim, Norway, peter.robinson@ngu.no
[2] Bayerisches Geoinstitut, Universität Bayreuth, D-95440 Bayreuth, Germany
[3] Norwegian University of Science and Technology, N-7491, Trondheim, Norway

* now at Institut für Geowissenschaften, Friedrich-Schiller-Universität Jena, 07745 Jena, Germany

Corresponding Author: Peter Robinson, peter.robinson@ngu.no

Abstract

Extensive negative aeromagnetic anomalies in the Modum area, south Norway derive from rocks containing ilmenite with hematite exsolution, or hematite with ilmenite exsolution, carrying strong/stable reversed remanence. Here we describe a 2.5-cm-thick high-temperature metamorphic vein of exsolved titanohematite. Reflected-light and EMP analyses show it contains three types of exsolution: spinel plates on (001); rutile blade satellites on spinel oriented at angles of ~60-90^{o} to titanohematite (001); and lamellae 0.1-0.3 μm thick too fine for EMP analyses, also parallel to (001). Powder XRD gave $\boldsymbol{a}$=5.0393 Å, $\boldsymbol{c}$=13.7687 Å, V=302.81 Å^3 for titanohematite (≈Ilm9), and unrefined reflections of rutile and geikielite. Overlap EMP analyses showed enrichment in MgO, TiO_2 and lack of Al_2O_3, indicating a mixture of titanohematite and geikielite. Non-overlap analyses showed the titanohematite is 6%$Fe^{2+}TiO_3$, 2%$MgTiO_3$, 92% Fe_2O_3, generally confirmed by TEM-EDX analyses that also showed the geikielite is 30%$Fe^{2+}TiO_3$, 70%$MgTiO_3$.

Orientation and interface relationships between exsolutions and host titanohematite were characterized with TEM, using conventional and high-resolution imaging complemented by selected area electron diffraction. As expected, spinel shares (111) with the (001) basal plane of titanohematite and geikielite (001) the same. The epitactic relationship between rutile and titanohematite, previously not well constrained, was estimated from reflected-light and TEM images and lattice-fit studies. The $\boldsymbol{a_1}$ axis of rutile is parallel to $\boldsymbol{a_1}$ of hematite and $\boldsymbol{c}$ of rutile is normal to $\boldsymbol{a_2}$ of hematite, all in the hematite basal plane, which, however is not a phase interface. The rutile appears to occur in blades within prism planes in titanohematite located ~69^{o} from $\boldsymbol{a}$ axes of hematite, with long axes of the blades oriented in a minimum strain direction within the planes at ~63^{o} from the (001) basal plane.

Spinel and rutile, analyzed by EMP, exsolved first. Spinel gave 96%$MgAl_2O_4$, 3%$FeFe_2O_4$, Mg/ total R^{2+} = 0.98. Magnesian/aluminous spinel lacking Ti exsolved from titanohematite in coupled exsolution with ferrian rutile, where combined components were dissolved as corundum/geikielite components in high-T aluminous magnesian titanohematite. Early exsolution

lowered geikielite, and eliminated the corundum component. Later fine exsolution of ferroan geikielite moved the titanohematite closer to Fe_2O_3.

Mg^{2+} has no magnetic moment, but breaks up linkages between Fe atoms, lowers Néel *T*s, and produces unusual low-*T* properties. This titanohematite has Néel *T*, 873K (600°C). Geikielite at 70%$MgTiO_3$, is far beyond its theoretical nearest-neighbor percolation threshold at 30.3%$MgTiO_3$. However, the sample shows a negative magnetic exchange bias below 25 K and low-*T* remanence lost above ~40 K. Such properties are reported in samples containing thin ilmenite lamellae in titanohematite, in theory with odd numbers of Fe layers, where exchange bias is linked to lamellar magnetism at the phase interfaces, when the ilmenite becomes a high-anisotropy magnet in a magnetically softer host. The behavior of the ferroan geikielite has three potential explanations, formation of Fe-rich Mg-impoverished "clusters" allowing local percolation and magnetic interaction with adjacent contact layers, increased magnetic interactions at low temperatures between non-nearest-neighbor Fe atoms, allowing ferroan geikielite to percolate magnetically in unexpected fashion, and exsolution of much finer Fe-richer ilmenite lamellae, so far undetected in TEM. (503 Words, limit is 800, but 250 recommended)

Introduction

Figure 1 shows magnetic anomalies over the Mesoproterozoic basement rocks of the Modum district, south Norway (inset Figure 1), and northwest margin of the Permian Oslo Rift that preserves Cambro-Silurian fossiliferous sedimentary strata cut by Permian intrusions, many in classic ring-dike complexes. In many locations the rift boundary (thin dashed black line) is an east-dipping normal fault, but locally in Figure 1, the boundary is a gently east-dipping unconformity. The underlying basement rocks show a north-northwest trending structural grain produced during early Sveconorwegian (~1092 Ma) deformation and amphibolite-facies regional metamorphism (Bingen 2008).

The aeromagnetic map shows areas of positive induced magnetization (red-lavender colors) and areas of magnetic lows (orange through dark blue). The orange-blue areas west of the rift

margin are areas dominated by negative remanent magnetization, reflecting, in part, the structural grain of titanohematite-bearing layers. These rocks have a reversed paleomagnetic vector with declination 276, inclination -67, reflecting the late Mesoproterozoic time of remanence acquisition. This vector is at a large angle to the present Earth field vector with declination 51°, inclination +72.5 ° and results in magnetic lows. The rift margin is poorly resolved, because it is mainly an unconformity. The positive anomaly in the northeast of the map is a mafic body in the basement that extends southeast beneath the unconformity under Lake Tyrifjorden. The main magnetic low in the southeast relates to the strong circular magnetic high associated with a Permian ring dike complex.

Our strategy has been to study aeromagnetic maps and related reports covering Proterozoic "basement" areas in Norway, Sweden, Australia, and the Grenville Province in eastern USA, and Canada. In these areas, negative magnetic anomalies quite commonly reflect substantial magnetic remanence. In many examples, such remanence, commonly related to the rhombohedral oxides hematite and ilmenite, proves to be very stable magnetically, commonly reflecting the orientation of the magnetic field at the time of cooling field millions or even billions of years before the present (McEnroe et al., 2001a, 2002, 2007a, 2007b, 2008, 2009; McEnroe & Brown 2001; Robinson et al. 2012). Because of their high stability, such rocks are an important and useful source of paleomagnetic data, but they have also proved to be valuable for their unusual magnetic properties, some of which may ultimately provide blueprints for technological applications (McEnroe et al. 2007a). The negative magnetic anomalies over the basement rocks of the Modum area have proved particularly fruitful in this respect.

Figure 1 shows ten localities where we have collected, mostly within significant negative anomaly areas. One (Mod-2) was the subject of a detailed study of low-temperature (*T*) magnetic exchange bias in titanohematite with 1-2 nm scale ilmenite exsolution lamellae (McEnroe et al. 2007a, Harrison et al. 2007, 2010; Fabian et al. 2008). The samples at Mod-22 (manuscript in preparation) also contain titanohematite with similar properties but with ilmenite lamellae so thin as

to be undetectable except by magnetic techniques. The present study is based on one sample collected at Mod-24.

Sample occurrence at Mod-24

The Mod-24 vein sample occurs in a north-northwest trending belt of metamorphosed stratified rocks marked by prominent negative magnetic anomalies. The outcrop is limited and we focused our attention on a north-south trending ridge west of a wood road, where an east-west ground-magnetic profile was measured before collecting samples from different layers. The magnetic profile shows two narrow, steep-sided moderate magnetic lows at 48,800 (W) and 49,100 nT (E) apparently associated with particular layers or groups of layers. The Earth field at this location had intensity 50,784 nT, higher than nearly all the measurements. The high-*T* metamorphic titanohematite vein, discussed here, was found on a very small, glaciated, outcrop surface near the east end of the traverse and on the eastern flank of the eastern anomaly. The ~2.5-cm-thick vein cuts through feldspathic gneiss that is not very magnetic.

Reflected-light microscopy

Figure 2 shows a polarized reflected-light photomicrograph of a part of the sample. The dominant hematite host shows light-gray reflectivity. The most prominent exsolved phase is spinel in thin plates parallel to (001) of the host (using 3 hexagonal indices in the 4 index system), showing black because of very low reflectivity. Commonly attached to these plates are blades or rods of rutile showing dark gray reflectivity. The blades or rods lie at angles of 60^{o} or greater to the spinel plates. Throughout the hematite host there are very thin lamellae of lower (gray) reflectivity parallel to (001) that have been identified as ferroan geikielite. Figure 2b is a close-up reflected-light image of spinel and tiny ferroan geikelite plates parallel to (001) of the titanohematite host and blades or rods of rutile formed as attachments to the spinel plates. The plates or rods make angles of $\approx 60^{o}$ to rarely 90^{o} to the spinel lamellae. The nearly constant association of spinel and rutile within this sample provided a necessary clue to the nature and sequence of exsolution reactions.

X-ray diffraction

An X-ray powder diffraction pattern was collected at the Bayerisches Geoinstitut, University of Bayreuth, using a Panalytical X'Pert Pro X-ray diffraction system operating in reflection mode at 40 kV and 40 mA equipped with a $CoK\alpha_1$ (λ = 1.78897 Å) radiation selected with a focusing monochromator, a symmetrically cut curved Johansson $Ge_{(111)}$ crystal, and with a Philips X'celerator detector. The diffraction pattern was analysed with a full pattern profile fitting refinement (Rietveld analysis) using the GSAS software package (Larson and von Dreele, 1994) and the Windows interface, EXPGUI (Toby, 2001). This showed a hematite host and traces of rutile and geikielite. The hematite gave the following refined lattice parameters: $\boldsymbol{a}$ = 5.0393Å, $\boldsymbol{c}$ = 13.7687Å, V = 302.81Å^3 compared to pure Fe_2O_3 with $\boldsymbol{a}$ = 5.038Å, $\boldsymbol{c}$ = 13.772Å, V = 302.72Å^3, pure geikielite with $\boldsymbol{a}$ = 5.0548Å, $\boldsymbol{c}$ = 13.8992Å, V = 307.56Å^3, and pure ilmenite with $\boldsymbol{a}$ = 5.0884Å, $\boldsymbol{c}$ = 14.0855Å, V = 315.84Å^3. The cell volume on our working curves suggests a composition ≈Ilm 0.09.

Electron microprobe conditions, standards

The instrument, instrument conditions, and standards for these are given in Table 1A.

TEM-EDX analyses

To analyze the chemical compositions of exsolutions and hosts we used an analytical Philips CM20 field emission gun (FEG) transmission electron microscope (TEM) at the Bayerisches Geoinstitut, University of Bayreuth. The TEM was operated at 200 kV. Compositions were determined by aid of an attached ThermoNoran energy-dispersive X-ray spectrometer (EDX). The EDX detector is equipped with an ultrathin window and a Germanium detector, allowing also the detection of the *k* lines of light elements including the oxygen *k* line. To determine the chemical compositions of exsolutions and host titanohematite we have calibrated the $k_{X/O}$ factors for the elements *X* contained using a set of oxide standards (Langenhorst et al. 1995). The quantification of analyses involved an X-ray absorption correction, which was based on the principle of electroneutrality, i.e. the thickness was varied until the charges of anions (oxygen) and cations balanced (Van Cappellen & Doukhan 1994). Errors in analyses result from uncertainities in *k*

factors and the counting statistics of analyses. The relative errors in *k* factors are 1–3 per cent and represent systematic errors in the quantification. EDX analyses were run for 3 minutes in order to obtain >10000 counts for major elements (O, Fe, Ti in titanohematite + Mg in geikielite). The resultant relative statistical errors expressed as a 1σ deviation are 0.5–1 per cent for major elements and 2–3 per cent for minor elements (Mg, Cr in titanohematite). Trace elements with a concentration smaller than 1 atom % are only considered as detected.

Results of chemical analyses

Electron microprobe analyses of spinel, rutile, and rhombohedral oxide are presented in Tables 1 and 2. Analysis of spinel without hematite overlap (Table 1) was possible because of the presence of a few blebs and wider lamellae. A typical composition formulated to a three-cation formula gives Al 1.925, Mg 0.986, Fe^{2+} 0.016, Fe^{3+} 0.067, Cr 0.002, Ti 0.003, Zn 0.001, Ni 0.001. In terms of general end-member compositions, this calculates to 96.3% $R^{2+}Al_2O_4$ (aluminous spinel) 3.3% $R^{2+}Fe^{3+}{}_2O_4$ (ferrite), and 0.3% $R^{2+}{}_2TiO_4$ (ulvöspinel) with a ratio $Mg/(Mg+ Fe^{2+}) =$ 0.984. It is interesting that such a composition, obviously exsolved in some way from hematite with only minor Al and Mg substitution, though substantial Fe^{2+} and Ti substitutions, could exsolve a phase dominated by Al and Mg, with very minor Fe^{3+} and trivial Ti.

Only rare places in rutile were wide enough to obtain reasonable electron probe analyses without overlap with the host (Table 1). A formulation to 1 cation gave 0.886 Ti, 0.087 Fe^{3+}, 0.021 V^{3+}, and 0.005 Mg. Fe has been formulated as Fe^{3+}, based on work of Bromiley et al. (2004) and Bromiley and Hilairet (2005), and V as V^{3+}. Very substantial charge imbalance shown by the formula could be partially relieved if V were taken as V^{5+}. According to Bromiley and co-authors, there are two likely ways toward balancing the charge of Fe^{3+} substitution, by oxygen vacancies and by placing (OH) for O in the formula. Their studies suggest the former mechanism is more closely coupled with Fe^{3+} substitution than the latter. One speculates that the latter mechanism could be important in a sample formed under amphibolite-facies conditions. Lacking information on oxygen vacancy, the latter mechanism was used for the formulae in Table 1. The results thus reflect a

maximal estimate of (OH) content. The composition should be described as ferrian rutile, and, because of its source as an exsolution product in hematite, is likely one of the more Fe-rich rutiles reported.

Among the rhombohedral oxide analyses, many can be shown to result from overlaps with spinel and rutile and were not treated further. The remaining analyses, with the best examples listed in Table 2, are plotted in Figure 3. Here the vertical axis is $2Ti /(2Ti+ R^{3+})$, which provides the total fraction of "ilmenite-like" component. Subtraction of this fraction from 1 gives the fraction of hematite component. The horizontal axis $Mg /[(R^{2+}+ (R^{3+}/2)]$, by its construction, gives the absolute value of the $MgTiO_3$ geikielite end-member component. The EMP analyses in Figure 3 show a cluster at and slightly below "ilm" 0.1, with a considerable tail up to about "ilm" 0.2, with "geikielite" up to just above 0.1, representing analyses where geikielite lamellae overlap with hematite. There are two more probable geikielite overlap analyses (not in Table 2 due to poor sums) with "ilm" near or slightly above 0.3 and "geikielite" just below 0.3. Using these two points and the geikielite-poor cluster as an anchor, a trend can be drawn, implying that the actual giekielite lamellae compositions are near "geikielite" 0.9.

Also plotted on Figure 3 are the TEM-EDX analyses performed on the hematite host areas between lamellae (Table 3) and on geikielite lamellae (Table 4) using an analytical spot size of about 10 nm. The TEM has the ability to measure in much smaller areas than the electron microprobe, but the counting statistics are less robust, and the spectral resolution is not so good (Langenhorst et al. 1995), making the detection and quantification of minor elements like Mg and Ti difficult. At the small scale of Figure 3, the TEM hematite analyses appear to fall quite close to the EMP hematite analyses, though closer inspection shows this is misleading. The TEM geikielite analyses, dominated by Mg and Ti show considerable scatter both above and below the horizontal line at "ilm" = 1.0, and also about a location on that line centered at "geikielite" 0.70, quite different from the position at 0.9 implied by the EMP trend. The reason for this difference is unclear, but we

feel that the TEM results, though scattered around "geikielite" 0.70 must be reasonably close to this value.

Figure 4 covers the hematite-rich part of Figure 3, extending only to "ilm" 0.2 and "geikielite" 0.2. Here the hematite-rich cluster and geikielite overlap tail of the spinel-free EMP analyses are well shown. This also shows that the more dispersed cluster of hematite TEM analyses falls outside the cluster of EMP analyses. Comparison of the results, suggests that some of the EMP analysis points are from areas where there were no geikielite lamellae. On this basis, the hematite host composition is quite confidently located at Hematite 0.92, Ilmenite 0.06, and Geikielite 0.02.

Secondary hematite-chlorite vein

The EBS image of Figure 5 shows one part of the sample where there is a clean cross-cutting secondary vein of Ti-free hematite about 200 μm thick. This is lined with plates of magnesian chlorite, that are lined up parallel to (001) of the host titanohematite. Analyses of this hematite are listed in Table 5 and plotted at exaggerated scale in the inset of Figure 4. This emphasizes the remarkable purity of the vein hematite. All analyses plot in the extreme lower corner, with a maximum "ilmenite" component of 0.002. Because the vein contains no Ti minerals at all, it seems likely that the vein was not produced by interaction of fluid with the host hematite but rather that constituents for the vein hematite and chlorite were introduced from an external source long after the high-grade regional metamorphism.

TEM imaging of exsolutions

To characterize the orientation relationships between exsolutions and host titanohematite (see also TEM-EDX analyses), we used the afore-mentioned CM20 TEM at the Bayerisches Geoinstitut, University of Bayreuth. The characterization of orientation relationships focused mainly on rutile exsolutions, as in the reflected-light images of Figure 2, where spinel and geikielite plates appear to be parallel to (001) of the hematite, whereas rutile blades or rods make angles of ≈ 60-90^{o} to the spinel lamellae. This epitactic relationship with titanohematite was so far not well

constrained. For this purpose we complemented conventional (bright-field – BF and dark-field – DF) and high-resolution imaging (HRTEM) techniques with selected area electron diffraction (SAED).

Crystallographic orientation of exsolutions in titanohematite

The intergrowth between two rutile exsolutions, a spinel blade, and the host titanohematite is visible in Figure 6. Figures 7a and 7b show the corresponding electron diffraction patterns in the same orientation of titanohematite and rutile. The zone axis patterns ([211] for titanohematite and [0 -1 1] for rutile) reveal the following orientation relationship:

$[-102]_{hematite}$ // $[011]_{rutile}$ and $[-120]_{hematite}$ //$[100]_{rutile}$.

These relationships are illustrated in the precisely oriented unit cell diagrams of Figure 8 based on the measured lattice parameters of titanohematite, $\boldsymbol{a}$ = 5.0393 Å, $\boldsymbol{c}$ = 13.7687 Å, and lattice parameters estimated for ferrian rutile based on ionic radii of the ions substituting for Ti^{4+}, a = 4.6218 Å, c = 2.7086 Å. Calculating from hematite parameters, the (blue) plane (-1 0 2) makes an angle 57.63° with the (001) basal plane. Calculating from rutile parameters, the (blue) plane (011) makes an angle 59.63° from the (010) bottom plane. In this relationship one $\boldsymbol{a}$ axis (here $\boldsymbol{a_2}$) of rutile is quasi-parallel to the $\boldsymbol{c}$ axis of titanohematite and the second $\boldsymbol{a}$ axis (here $\boldsymbol{a_1}$) of rutile is parallel to one $\boldsymbol{a}$ axis (here $\boldsymbol{a_2}$) of titanohematite. The latter can be directly seen in the high-resolution TEM image (Figure 9). This rational orientation relationship means also that the hexagonal close packing (hcp) of oxygen is retained between the two phases (titanohematite: hcp // (001); rutile: hcp // (010)).

Spinel is commonly known to possess an orientation relationship with [111] being parallel to [001] of titanohematite. In this way, the close-packed layers of oxygens in both structures are parallel to each other. The plane of interface between the two phases can be determined from Figure 6 by taking the width of the fringe pattern (about 200 nm) on the side of the spinel blade and assuming a typical thickness of the foil of about 100 nm. Taking these values, one can calculate that the plane of interface is about 60° inclined to the beam direction, i.e. [211] of titanohematite (Figure

7a). Furthermore, we see in Figure 7a that the $\boldsymbol{a_2}$ axis of titanohematite is quasi-parallel to the trace of the spinel blade, thus demonstrating the comprehensive relationship between the two phases and the TEM foil shown in Figure 10. A rotation of about 60° about $\boldsymbol{a_2}$ would bring the (001) plane edge-on. Thus, the plane of intergrowth is (001) for titanohematite and (111) for spinel. Because geikelite possesses the same structure as titanohematite, the lattices of both phases are in the same orientation.

The plane of intergrowth between titanohematite and rutile is more difficult to determine, because, first, the interface is not exactly edge-on in the projection of the [211] zone axis (Figs. 6 and 7) and, secondly, the limited tilting capabilities of the TEM did not make it possible to orient the beam along the ***c*** axis of titanohematite (being 32° away from [211]). A recent study (Daneu et al., 2007, their Figure 10) provided insights into the relationships between rutile and ilmenite when (1) an interface between the two phases is seen edge-on, (2) the *c* axis of the rhombohedral phase is along the beam and (3) the *c* axis of rutile is perpendicular to it, as in our sample. They identified an interface as (310) rutile parallel to a prism plane (100) of ilmenite (thus parallel to $\boldsymbol{a_2}$). The rutile c axis was inclined to the interface by 30°, thus making an angle of 30^o with the ilmenite ***a2*** axis. By contrast, in our sample, the rutile ***c*** axis makes an angle of 90^o to the **a2** axis of hematite. In Figure 9, the trace of the rutile-hematite interface makes an angle of about 75° to the ***a2*** axis of hematite, also the ***a1*** axis of rutile, suggesting a prism plane of intergrowth (h01) with h>3. A similar interface between rutile and hematite can be seen on the right hand side of Figure 6, where it is ~75^o from the trace of spinel (but not exactly to ***a2***, see below). In Figure 9 the interface is also inclined by an uncertain amount in a direction normal to the image.

A complication in making interface angle measurements in Figures 6 and 9 is that both images show angles in the plane of the TEM foil, which is tilted approximately 58^o from the proposed prism planes, and the axis of tilting is not necessarily parallel to the ***a2*** axis. Assuming 58^o tilting is parallel to ***a2***, a true prism angle yields an apparent prism angle about 2^o larger, thus for 72^o true, 74^o apparent; for 69^o true, 71^o apparent. However, in cases where the foil is not tilted

parallel to a2, but on an axis at an angle to ***a2***, the two apparent angles are not symmetric. For a true angle 69^{o} with tilting about an axis 4^{o} from ***a2***, the resulting angles are ~68^{o} and ~75^{o}, and slight tilting in other directions will similarly alter apparent angles. With these complications in mind, measurements of the angle between ***a2*** in the combined Figures 6 and 7 yielded 68^{o} to the left and 73^{o} to the right, and caused us to select 69^{o} as the best prism angle.

The information derived from Figures 6, 7, 8, 9 can be used to understand the orientation of the elongate rutile blades or rods, which cannot be parallel to ***c*** of rutile, which is parallel to the hematite basal plane (Figure 8). The study by Daneu et al. (2007) suggested that a promising interface direction would lie in a prism plane parallel to ***c*** of the rhombohedral phase. Observation of Figure 9 indicated a probable interface orientation about 75^{o} from ***a2***, subject to the fact that this interface segment may not be strictly parallel to the interface over a larger interface distance. To simplify efforts to determine lattice best fits between the two phases, we reduced both sets of lattice parameters to equivalent rhombohedral cells (easy to visualize in Daneu et al.'s Figure 10) and also gave the cells initially a common orientation along non-crystallographic x, y, and z axes. For titanohematite we used our measured lattice parameters. For rutile we corrected the lattice parameters to account for the substitution of cations larger than Ti^{4+}, namely Fe^{3+}, V^{3+} and Mg^{2+} as reported in Table 1.

For titanohematite:	**For ferrian rutile:**
Along x: ***a*** tan 30^{o} = 2.09944 Å	Along x: ***c*** = 2.70862 Å
Along y: ***a2*** = 5.0393 Å	Along y: ***a1*** = 4.6218 Å
Along z: ***c*** = 13.7687 Å	Along z: 3 x ***a2*** = 13.86528 Å

Assuming a prism plane interface, one first seeks a minimum strain plane using only the x and z values of the equivalent-cell parameters as in Figure 11a,b. Here rutile is consistently smaller than hematite, hence under tension. The lattice points of both phases, without any rotation, lie very close to a line passing through coordinates 0, 0 and 9, 2. This makes the angle 69 +/- 0.15^{o} with the y coordinate direction (also an ***a*** direction of both phases).

One next examines relations within the prism plane illustrated in Figure 11c,d. In doing this the diagonal distance within the x, y plane is compared against the different distances in the z direction, where rutile is slightly larger tha hematite. By rotating the rutile lattice only 2^{o} clockwise Figure 11d) or counter clockwise (Figure 11c), a good lattice fit is obtained between the two phases. At the lattice point 9, 2, 4 in 3-D in (Figure 12a), the x and z coordinates for rutile compared to hematite ( ) are 25.9703 Å (26.1850) and 55.5494 Å (55.0748) in good agreement. There is no change in the y coordinate, because the rotation is about the y axis parallel to the common ***a*** axes,. not about a line normal to the prism plane.

A more direct solution can be obtained from the TEM results in Figures 7 and 8, wherein the two phases share a common lattice plane (-1 2 0) for titanohematite and (011) for rutile. From the lattice parameters, the titanohematite (001) basal plane lies 57.63^{o} from the common plane, whereas (010) of rutile lies 59.63^{o} from the common plane. This, in turn, means that the ***c*** axis of rutile is rotated 2^{o} counterclockwise (see Figure 11c) about the common ***a*** axes from the ***c*** axis of titanohematite. This is geometrically identical to the 2^{o} clockwise rotation calculated from Figure 12a, through equations.

The sense of the above results is shown in Figure 12b, based on the 9 x 2 x 4 cell model. Within the geometrically equivalent titanohematite block, there are two best-fit prism planes (red and purple) both at 69^{o} to the common ***a*** axes, and each containing two diagonal best-fit lines. The best-fit lines to the right involve clockwise rotation of rutile ***c*** axes about the common ***a*** axes to achieve best fit (the red one modeled in Figure 12a). The diagonal best fit lines to the left involve counterclockwise rotation of rutile ***c*** axes about the common ***a*** axes. Counterclockwise rotation is the one actually observed in the right area of the TEM image of Figure 6, involving the rutile blade in the diffraction image of Figure 7b (left red blade in Figure 12b). The same rotation can involve also the rutile blade in the left area of Figure 6 (left blue blade in Figure 11b), though that is not yet proved by selected area diffraction. If true, then both blades in Figure 6 would have long axes that 'plunge' to the right with respect to the foil surface.

There is another aspect of the high-resolution image in Figure 9 not yet explained. Although the lattice planes normal to the mutual hematite $\boldsymbol{a_2}$ and rutile $\boldsymbol{a_1}$ axes are perfectly parallel, the lattice planes in rutile that should be parallel to $\boldsymbol{a_1}$ are in fact misoriented counterclockwise by about 2°, so that the crystallographic $\boldsymbol{a_1}$ axis and [0-1-1] direction are not at 90°, but at ~92°. This discrepancy cannot be related to the lattice rotations described above because the interface is at a high angle (estimated 84°) to the foil so that such rotations could not be observed. The true explanation for this seems to be in the strong lattice strain along the rutile blade edges. This is obvious in Figure 11a and b, where the amount of interface stretch of rutile increases dramatically away from the blade axis with increasing distance from the anchoring points, where growth presumably started, in these lattice views. For Figure 9, then, one can conclude that the anchoring point for this particular rutile blade, likely a location where exsolution was initiated, lies to the right, so that the hematite host is causing a sinistral shear (in this view) in the adjacent rutile.

The overall result of these considerations is that the rutile appears to have grown in blades or rods within prism planes parallel to $\boldsymbol{c}$ and at 69° to the $\boldsymbol{a_2}$ axis of hematite, and elongated along best fit lines that lie at 63° to the hematite (001) basal plane. Furthermore, all the different rutile orientations with different lattice and interface orientations with respect to hematite, can be accommodated within the confines of a single titanohematite single crystal. The different rutile lattice and interface orientations would then have been initiated locally at the beginning of coupled exsolution. These conclusions are illustrated for a more extensive array of planes and lines in Figure 13. Figure 13a shows positions of prism best-fit planes for rutile in hematite oriented at angles of 69° to each of the $\boldsymbol{a}$ axes. Figure 13b shows positions of three rutile blades oriented along one best fit line in each of three planes in (a). Based on the synthetic lattices, there might be two such lines in each prism plane, thus giving twelve possible orientations. That number could be reduced based on interface details not explored in the simplified model. Also the number of blades visible near given surfaces may be greatly reduced compared to the total number present. Note that the back two prism planes in Figure 13c lie at 138° from each other. In Figure 6 the two rutile

blades are separated by 141°, the difference being due to different viewing angle. All these results are entirely consistent with observations in reflected-light and in EBS images. Local deviations in observed angles will depend on the exact angle of the surfaces on which measurements are made.

Chemography for the nature and sequence of exsolution

Figure 14a illustrates the nature of a low-*T* reaction in the system FeO-Fe_2O_3-TiO_2 (Lindsley 1991) as expressed by the cation proportions of Fe^{2+}, Fe^{3+}, and Ti^{4+}. At low *T*, below approximately 400°C, coexisting ilmenite + titanohematite react to produce the assemblage magnetite + rutile. Two previous three-phase equilibrium triangles ilmenite-hematite-rutile and ilmenite-hematite-magnetite are then replaced by two new three-phase equilibrium triangles ilmenite-rutile-magnetite and hematite-rutile-magnetite. In the new ilmenite assemblage, with further cooling, the ilmenite would lose hematite component, producing more rutile and magnetite. In the new hematite assemblage, with further cooling, the hematite would lose ilmenite component, also producing more rutile and magnetite. These reactions provide inspiration for explaining the Mod-24 sample, because they show how rhombohedral oxides can break down to an equivalent amount of a spinel mineral and rutile.

To follow this reaction more closely, consider breakdown of the rhombohedral oxide exactly intermediate between ilmenite and hematite to yield magnetite + rutile, according to the reaction 1.0 $Ilmenite_{50}Hematite_{50}$ = 0.50 Magnetite + 0.50 Rutile. The stoichiometric reaction is 1 $(Fe^{2+}_{0.5}Ti_{0.5}Fe^{3+}_{1}O_3)$ = 0.50 $(Fe^{2+}Fe^{3+}_{2}O_4)$ + 0.50 TiO_2 , or in cation terms $Fe^{2+}_{0.5}Ti_{0.5}Fe^{3+}_{1}$ = $Fe^{2+}_{0.5}Fe^{3+}_{1}$ + $Ti_{0.5}$. The relative volumes of the product magnetite and rutile can be estimated from the proportions of oxygen of these two phases, which is 4/2, or double the volume of magnetite compared to rutile. The intermediate rhombohedral oxide reactant may be thought of as the "extracted component" from rhombohedral oxide used to produce magnetite and rutile.

The relationships in Figure 14a are used in Figure 14b to consider reactions in a wider chemical system, with Mg, Zn, and Ni added to the Fe^{2+} apex, and Al, V^{3+} and Cr added to the Fe^{3+} apex. Here, we place Mg-spinel in the previous position of magnetite, and show rutile with its

ferrian component. One can then examine a reaction where an aluminous magnesian component is extracted from high-*T* aluminous magnesian hematite to produce a new titanohematite closer to end-member composition, plus magnesian spinel and ferrian rutile. The composition of the extracted component necessarily lies on the spinel – rutile tie line in Figure 14b. Its composition is estimated by the reaction 0.9685 aluminous magnesian titanohematite component = 0.4685 magnesian spinel + 0.5315 ferroan rutile (see Appendix), based on the analyses of the spinel formulated to 3.000 cations and rutile formulated 0.999 cations. The aluminous magnesian titanohematite is a fictive extract component, but, in the Appendix, is normalized to a standard 2 cation rhombohedral oxide formula. Relative volumes of product spinel and rutile are estimated from relative proportions of oxygen of these two phases, which is 3.75/2.13, or 1.76 times the volume of spinel compared to rutile. The lower proportion of spinel compared to magnetite (compare Figures 13a and 13b), is easily understood using the lever rule.

The simplified compositions (omitting V_2O_3) are used in the tetrahedron in Figure 15 to show the entire exsolution sequence during cooling from peak amphibolite-facies conditions. An original high-*T* aluminous magnesian titanohematite yielded an extracted component near the Fe^{3+}-free plane, which formed spinel + rutile. The extraction drove the residual titanohematite composition to the Al-free plane, which has the same topology and orientation as Figure 3. Further cooling widened the miscibility gap between titanohematite and the ilmenite-geikielite series. Fine lamellae of ferroan geikielite of compositon "geikielite" 0.70 separated, driving the hematite to its final composition Fe_2O_3 0.92, $FeTiO_3$ 0.06, $MgTiO_3$ 0.02. The final analyses show a significant fractionation of Mg under these conditions between geikielite with $Mg/(Mg+ Fe^{2+}) = 0.70$ and titanohematite with $Mg/(Mg+ Fe^{2+}) = 0.25$. The shape shown for the miscibility gap between titanohematite and ilmenite-geikielite is speculative. An exhaustively calculated view of this is provided by Ghiorso (1990), including evidence for an incipient ilmenite-geikielite miscibility gap at low *T*.

Magnetic properties

435 The magnetic properties of this sample are dominated by the titanohematite host. Minor
436 substitutions of $FeTiO_3$ and $MgTiO_3$ are sufficient to suppress a Morin transition. It is challenging
437 to determine whether any of the magnetic properties measured can be assigned to the ferroan
438 geikielite exsolution lamellae. Mg^{2+} is not a paramagnetic ion, i.e. it contains no unpaired d-orbital
439 electron spins and creates no exchange coupling. In ferroan geikielite it essentially dilutes the
440 network of magnetic exchange interactions between the Fe^{2+} ions. We assumed the spinel and
441 ferrian rutile are not significantly magnetic. Rutile blades passing through antiferromagnetically
442 coupled layers parallel to (001) in the host, at best, could create a type of magnetic interface
443 moment.

444 In the case of magnetic interactions in the ilmenite structure at 57 K and below (Burton et al.
445 2008; Robinson et al. 2010), there are relatively weak double-layer antiferromagnetic interactions
446 which cause the magnetic moments to be opposite along $\boldsymbol{c}$ in alternating Fe^{2+} layers. In addition,
447 strong ferromagnetic interactions within each Fe^{2+} layer cause all the moments to be oriented in the
448 same direction within the layer. Mathematical analysis (Ziff and Gu, 2009) of a hexagonal network
449 of points, such as that of Fe^{2+} ions in the (001) plane of ilmenite, indicates a site percolation
450 threshold of 0.6970 for this strong interaction, meaning that nearest-neighbor magnetic exchange
451 coupling would require that at least 69.7% of sites to be occupied by Fe^{2+} to generate an infinite
452 percolating cluster within this plane, hence not more than 30.3% Mg replacement of Fe^{2+}. This
453 suggests that the ferroan geikielite lamellae discussed here, with ~70% Mg replacement, should not
454 show global antiferromagnetic ordering at any *T*. However, low-*T* magnetic experiments described
455 below show that the geikielite lamellae have a significant magnetic expression below 40 K, and
456 strongly affect the bulk magnetic properties at *T*s below 25 K.

457 In the case of FeTi-ordered hematite-ilmenite solid solutions, the situation is different,
458 because Fe^{3+} ions are equally distributed between adjacent cation layers even where Fe^{2+} and Ti^{4+}
459 are not, and also Fe^{3+} interactions between adjacent layers are very much stronger than the double-
460 layer interactions in the ilmenite structure (Robinson et al. 2010). This means that adjacent-layer

interactions can percolate in the end-member system until ~X Ilm = 0.87 (Burton et al. 2008). Mg substitution in the ilmenite component, lowers the percolation threshold somewhat, but far less significantly than in the ilmenite-geikielite series. In addition, at very Ti-rich compositions, we know that a small amount of hematite substitution lowers the Néel *T* of antiferromagnetic ilmenite (McEnroe et al. 2007b, Burton et al. 2008), but have been less sure if Mg substitution has a greater or lesser effect. Magnetic measurements of Mg-substituted and hematite-substituted ilmenite-rich compositions (Table 6) show a decrease in Néel *T*, but the details of Mg effects are a subject for future work.

The Néel temperature (T_N) of the titanohematite was determined by measuring saturation magnetization (M_s) and remanence saturation (M_{rs}) with temperature from 25 – 700C after the method of Fabian et al. (2013), which yields a much more precise result than earlier methods for determining T_N or Curie *T*. At each temperature the upper branch of the hysteresis loop up to 1.5 T is measured. From this M_s is estimated by extrapolating the linear high-field part to H=0. M_{rs}, is determined from a measurement in zero field. The resulting M_s and M_{rs}-*T* curves are shown in Figure 16. From the measured hysteresis branches, it can be inferred that the apparent drop in $M_s(T)$ below 200°C is an artifact due to insufficient saturation of the sample within the maximum measurement field of 1.5 T. Both curves give a T_N of 600°C (873 K), clearly below the value of 680°C (953 K) for pure Fe_2O_3. Our corrected polynomial fit of composition versus T_N for the entire hematite-ilmenite system indicates a composition X Ilm = 0.12 for T_N (873 K), compared to chemical results X $FeTiO_3$ = 0.06, X$MgTiO_3$ = 0.02. However, this part of the polynomial curve appears unreliable in that the pure Fe_2O_3 end is anchored at a *T* above 953 K, suggesting a better estimate at X Ilm = 0.10.

The visibly insufficient saturation complicates the estimation of M_s(30°C). Therefore, we first determined M_s (220°C) = 2332 A/m based on a density of 5219 kg/m^3. Because Ilm20, the hematite-ilmenite solid solution for which we have a measured M_s (T) curve with a T_N closest to Mod-24, shows a 12% drop in M_s between 30°C and 220°C we used this value to estimate

M_s (30°C) = M_s(220°C)/0.88 = 2650 A/m. The literature value for the spin-canted magnetization of pure hematite according to Morrish (1994) is M_s(30°C) = 2100 A/m. In our case this should be reduced by 5-8% to allow for 6% $FeTiO_3$ and 2%$MgTi0_3$ substitution in agreement with the lower T_N. Thus the expected M_s(30°C) for a diluted hematite would be 1995 to 1932 A/m. On this basis, 75-73% of the magnetization could be explained by the hematite, indicating the presence of 25-27% of an additional component.

In previous measurements on exsolved samples, where we knew that a fraction of the hematite magnetism was due to lamellar magnetism, and we had direct composition estimates of hematite composition (McEnroe et al. 2001b, 2002, 2007, McEnroe &Brown, 2001), T_N was consistently above the corrected curve. Here there is the question of whether there is, or is not lamellar magnetism at room *T* in this sample. This depends on whether the contact layer compositions, brought about to improve charge imbalance, contain enough Fe to couple magnetically to their adjacent hematite layers. A contact layer composition is determined by averaging the compositions of a disordered hematite layer and an ilmenite Fe-layer (Robinson et al. 2002, 2004), as indicated for Mod-24 below.

Disordered Hematite Layer	0.01 Mg	0.03 Fe^{2+}	0.04 Ti	0.92 Fe^{3+}
Ferroan Geikielite “Fe” Layer	0.70 Mg	0.30 Fe^{2+}		
Totals	0.71 Mg	0.33 Fe^{2+}	0.04 Ti	0.92 Fe^{3+}
Contact Layer Composition	0.355 Mg	0.165Fe^{2+}	0.02 Ti	0.46 Fe^{3+}

The calculated total Fe fraction of a contact layer is 0.625, within the percolation threshold for adjacent-layer magnetization. One can speculate as to whether a contact layer composition, with such a reduced Fe content, would influence the temperature of acquisition of the lamellar magnetism, nominally controlled by the hematite host. One may also speculate if such a composition at phase contacts could have some influence on low-*T* magnetic exchange bias.

Because of the substantial calculated Mg content of a contact layer against geikielite, the theoretical net magnetic moment at 0 K is much lower than when a contact layer is against end member ilmenite.

Magnetic Moment of Hematite Layer 0.03 x 4 = 0.12 μB 0.92 x 5 = 4.6 μB Total 4.72 μB

Magnetic Moment of Contact Layer 0.33 x 4 = 0.66 μB 0.46 x 5 = 2.3μB Total 2.96 μB

Magnetic Moment of One Lamella 2 x 2.96 = 5.92 μB 5.92 μB – 4.72 μB = **1.2 μB**

The resulting formal lamellar moment is only 1.2 μB compared to 4 μB for the example of pure $FeTiO_3$ exsolved from Fe_2O_3. This may be sufficient to explain the additional component detected in the Ms measurement.

After applying a field of 1.5T, then cooling in zero field, twenty-five hysteresis loops were measured on warming between 10 K and room-*T*. Shown in Figure 17 are two hysteresis loops measured at 300 K (a) and at 10 K (b). The room-*T* loop shows a typical rhombohedral oxide shape with an Mrs/Ms ratio of 0.70, which is significantly higher than the maximum of Mrs/Ms= 0.50 expected in a random uniaxial single-domain magnetite ensemble. The bulk coercivity of Hc= 43 mT is larger than that of a typical multi-domain hematite, which has Hc< 10 mT, and results from the abundant fine exsolution lamellae. At low-T the 10 K loop is remarkable in that it shows a negative exchange bias with a shift of -40 mT. From 10 K to 25 K the loops remain shifted with decreasing amounts. At *Ts* above 25 K no shift is evident and the loops are symmetrical about the origin. Such shifts have now been well documented in hematite-ilmenite intergrowths (McEnroe et al. 2007) and understood on a theoretical basis (Harrison et al. 2007, 2010, Fabian et al. 2008) in hematite containing fine-scale exsolution lamellae of ilmenite, in which a significant magnetic moment only occurs in lamellae with an odd number of Fe layers. These shifts occur in cases when there is strong magnetic coupling across phase interfaces between a magnetically hard phase (ilmenite) and a magnetically soft phase (hematite), in which the contact layers of lamellar magnetism play a crucial role. The necessity of having two stable magnetic phases interacting across an interface to produce the shifted hysteresis loop, leads to the tentative conclusion that the

537 geikielite lamellae, despite their non-percolating nearest-neighbor exchange interactions, are
538 carrying a significant magnetic moment at very low *Ts*.

539 Figure 18 shows the results of a warming experiment measured in zero-field after first
540 applying a magnetic field of 1.5 T at 8 K. A steep decrease in magnetization between 8 and 25 K
541 corresponds to the interval in which there is the loss of the negative exchange bias of Figure 17B,
542 here tentatively attributed to ferroan geikielite-hematite interfaces. The plateau edge at ~40 K
543 corresponds in other samples to the conditions where ilmenite magnetization begins to decline, and
544 presumably here could correspond to a *T* where geikielite transforms from a nominally AF phase to
545 a paramagnetic phase and thus loses its magnetization.

546 What, then, can we understand about the magnetization of geikielite in a situation where
547 nearest-neighbor magnetic percolation is not possible? One possibility is that, even without
548 complete percolation through the major magnetic interactions, there are sufficiently large Fe-rich
549 Mg-depleted clusters to allow very local double-layer magnetizations to occur. This may create a
550 significant hard magnetic moment in geikielite which is coupled, through the more Fe-rich contact
551 layers, to the titanohematite. Another possibility is that at low-*T*, non-nearest neighbor interactions
552 become important. These could either allow a different path of percolation in geikielite, not
553 predicted on a theoretical basis from the nearest-neighbor interactions, or provide a random
554 exchange coupling network with spin-glass properties. A third possibility is that at very low *T* the
555 contact layers themselves, with their higher Fe content than the geikielite, interact independently
556 with the adjacent hematite. A fourth possibility is that, at a finer scale not yet resolved in TEM,
557 there are ilmenite lamellae more Fe-rich than those measured by the TEM-EDX analyses. Based on
558 our composition estimates for the titanohematite host, there is not a chemical possibility to produce
559 such lamellae in abundance, even in the unlikely case that it could be predicted from the chemical
560 phase relations (Figure 15).

561 **Implications**

562 The results of this study demonstrate the value gained from examination of areas of
563 remanent magnetic anomalies over igneous and metamorphic rocks in the search for magnetic
564 oxides with unusual compositions and exsolution intergrowths, where the magnetic interactions on
565 phase interfaces create special properties. Exsolution of high-temperature mineral solid solutions to
566 two phases of different composition, but identical structure, is the simplest phenomenon that can
567 occur during slow cooling. However, more complex phenomena are widespread and may include
568 exsolution of two phases with closely related but different structures, for example hematite and
569 ilmenite, or of phases with entirely different structure, such as pyroxene and ilmenite, etc.
570 Exsolution may occur within a material of constant composition, or may occur because of a change
571 of composition driven by an external chemical input. The classic example of the latter is the so-
572 called "oxy-exsoluton" of titanomagnetite to produce lamellae of ilmenite.
573 In the example described here, an initial high-*T* aluminous magnesian titanohematite, which
574 might have exsolved isostructural corundum, did not do so, but instead produced a coupled epitaxial
575 intergrowth of magnesian spinel and ferroan rutile, effectively extracting all Al and considerable
576 Mg and Ti from the host. After this, there was a second more simple phase separation of structurally
577 related ferroan geikielite (X $MgTiO_3$ = 0.70), further reducing Ti and Mg in the host to its final
578 composition X Fe_2O_3 = 0.92, X $FeTiO_3$ = 0.06, X $MgTiO_3$ = 0.02. These coexisting oxides provide
579 new insights into the stability of oxide phase assemblages and element fractionation between
580 phases.
581 Orientations of phase interfaces produced during exsolution are of considerable interest,
582 particularly when the interfaces are not along simple or rational directions, requiring close study.
583 Here we found that spinel (111) and geikielite (001) make simple interfaces with titanohematite
584 (001). By contrast, using combined techniques, it was found that rutile forms blades within the
585 titanohematite host that are not oriented in a simple rational direction of either, but do lie within
586 prism planes of minimal tensional strain and, particularly, are elongated along lines of least strain at
587 about 63^o to the titanohematite (001) plane. These directions are achieved by the rotation of rutile

lattice directions by 2°, as directly determined in selected area electron diffraction images, documenting an example where a misorientation of two lattices by this small amount, accommodates growth of interfaces in apparently irrational directions. This approach may apply to the many other examples of rutile hosted in rhombohedral oxide.

The special exsolution intergrowth of ferroan geikielite with titanohematite provides a surprising new insight into the theory of 'lamellar magnetism'. This would normally involve ilmenite ($FeTiO_3$) and hematite (Fe_2O_3), but here 70% of the Fe^{2+} of the ilmenite is replaced by Mg. Formal percolation theory suggests that nearest neighbor exchange interaction in this ferroan geikielite could not lead to an antiferromagnetic transition. Here we observed lamellar magnetism below 600°C, and, at 10 K, a significant negative magnetic exchange bias of 40 mT is shown in hysteresis measurements, demonstrating magnetic coupling via the "contact layers" of lamellar magnetism across phase interfaces between titanohematite and ferroan geikielite. This work indicates the possible presence of complex chemical clusters, non-nearest neighbor exchange coupling, spin-glass behavior, or low-*T* behavior of contact layers. It points the way toward more magnetic study of synthetic samples in the systems $FeTiO_3$-$MgTiO_3$ and Fe_2O_3-$MgTiO_3$.

Acknowledgements

Work by Robinson and McEnroe at University of Bayreuth, 2006-2008, was supported by an EU Access to Infrastructures Grant administered by Bayerisches Geoinstitut. This and related research was supported by grant 189721 from the Research Council of Norway (Nanomat Program) in the EU Matera Program, a Marie Curie Fellowship for McEnroe at Bayerisches Geoinstitut (GA-2009-237671), and visiting fellowships to the Institute of Rock Magnetism, which is supported by an NSF Instruments and Facilities Grant. Financial support was also provide by the Deutsche Forschungsgemeinschaft (LA 830/14-1). EMP analyses and key information for interpretation were provided by M. J. Jercinovic, University of Massachusetts, Amherst. The manuscript was improved by suggestions from two reviewers. To each of these persons and institutions we extend our grateful acknowledgement.

Appendix – Determination of extracted component

Spinel: 1.925 Al, 0.986 Mg, Fe^{2+} 0.016, Fe^{3+} 0.067, Cr 0.002, Ti 0.003, Zn 0.001, Ni 0.001 with simplified composition $R^{2+}Al_2O_4$ (aluminous spinel) 96.2%, $R^{2+}Fe^{3+}{}_2O_4$ (ferrite) 3.3%, $R^{2+}Cr_2O_4$ (chromite) 0.1%, $R^{2+}{}_2TiO_4$ (ulvöspinel) 0.3%.

Rutile: Ti 0.886, Fe^{3+} 0.087, V^{3+} 0.021, Mg 0.005.

"Extracted" rhombohedral oxide component: This sums to 1.93695 cations from the balanced reaction, but is normalized to 2 cations for a standard rhombohedral oxide formulation, thus, 0.931 Al, 0.488 Ti, 0.480 Mg, 0.080 Fe^{3+}, 0.012 V^{3+}, 0.001 Cr, 0.008 Fe^{2+} with simplified composition Al_2O_3 (corundum) 46.6%, Fe_2O_3 (hematite) 4.0%, V_2O_3 (karelianite) 0.6%, $MgTiO_3$ (geikielite) 48.0%, $FeTiO_3$ (ilmenite) 0.8%.

REFERENCES

Ancey, M., Bastenaire, F. and Tixier, R. (1978) Applications of statistical methods in microanalysis. In F. Maurice, I. Meny, and R. Tixier, Eds., Microanalysis and scanning electron microscopy. Proceedings Summer School St. Martin-d'Heres, Les Editions de Physique, Orsay, France, p. 319-343.

Bingen, B., Davis, W.J., Hamilton, M.A., Engvik, A., Stein, H.J., Skår, Ø., and Nordgulen, Ø. (2008) Geochronology of high-grade metamorphism in the Sveconorwegian belt, S Norway: U-Pb, Th-Pb and Re-Os data. Norwegian Journal of Geology, 88, 13-42.

Brok, E., Sales, M., Lefmann, K., Kuhn, L. T., Schmidt, W. F., Roessli, B., Robinson, P., McEnroe, S. A., and Harrison, R. J. (2014) Experimental evidence for lamellar magnetism in hemo-ilmenite by polarized neutron scattering**.** Physical Review B, 85, 054430-054437. 10.1103/PhysRevB. 89.054430.

Bromiley, G.D. and Hilairet, N. (2005) Hydrogen and minor element incorporation in synthetic rutile. Mineralogical Magazine, 69, 345-358.

Bromiley, G.D., Hilairet, N. and McCammon, C. (2004) Solubility of hydrogen and ferric iron in rutile and TiO2 (II): Implications for phase assemblages during ultrahigh-pressure

metamorphism and for the stability of silica polymorphs in the lower mantle. Geophysical Research Letters, 31, L04610 1-5.

Burton, B.P., Robinson, P., McEnroe, S.A., Fabian, K. and Boffa Ballaran,T (2008) A low-temperature phase diagram for ilmenite-rich compositions in the system Fe_2O_3-$FeTiO_3$. American Mineralogist, 93, 1260–1272.

Daneu, N., Schmid, H., Recnik, A. & Mader, W. (2007) Atomic structure and formation mechanism of (301) rutile twins from Diamantina (Brazil). American Mineralogist, 92, 1789-1799.

Fabian K., McEnroe, S.A., Robinson, P. and Shcherbakov, V.P. (2008) Exchange bias identifies lamellar magnetism as the origin of the natural remanent magnetization in titanohematite from ilmenite exsolution, Modum, Norway. Earth and Planetary Science Letters, 268, 339-353.

Fabian, K., Shcherbakov, V.P. and McEnroe, S.A. (2013) Measuring the Curie temperature. Geochemistry, Geophysics, Geosystems, 14, 947–961, doi:10.1029/2012GC004440

Ghiorso, M.S. (1990) Thermodynamic properties of hematite-ilmenite-geikielite solid solutions. Contributions to Mineralogy and Petrology, 104, 645–667.

Harrison, R.J., McEnroe, S.A., Robinson, P., Carter-Stiglitz, B., Palin, E.J. and Kasama, T. (2007) Low-temperature exchange coupling between Fe2O3 and FeTiO3: Insight into the mechanism of giant exchange bias in a natural nanoscale intergrowth. Physical Review B, 76: 174436, 10 pp.

Harrison, R.H., McEnroe, S.A., Robinson, P. and Howard, C. (2010) Spin orientation in a natural Ti-bearing hematite: Evidence for an out-of-plane component. American Mineralogist, 95, 974-979.

Langenhorst, F., Joreau, P., and Doukhan, J.C. (1995) Thermal and shock metamorphism of the Tenham meteorite: A TEM examination. Geochimica et Cosmochimica Acta, 59, 1835-1845.

Larson, A.C., Von Dreele, R.B. (2004) General Structure Analysis system (GSAS). Los Alamos National Laboratory Report LAUR 86-748.

665 Lindsley, D. H. (1991) Experimental studies of oxide minerals. In D.H. Lindsley, Ed., Oxide
666 minerals: Petrologic and magnetic significance. Reviews in Mineralogy, 25, 69-106,
667 Mineralogical Society of America, Washington, D. C.
668 Lutro, O. and Nordgulen, Ø. (2004) Oslofeltet, bergrunnskart M 1:250.000. Norges geologiske
669 undersøkelse.
670 McEnroe, S.A. and Brown, L.L. (2000) A closer look at remanence-dominated anomalies: Rock-
671 magnetic properties and magnetic mineralogy of the Russell Belt microcline-sillmanite gneisses,
672 Northwest Adirondacks Mountains, New York. Journal of Geophysical Research, 105, 16,437-
673 16,456.
674 McEnroe, S.A., Robinson, P. and Panish, P. (2001a) Aeromagnetic anomalies, magnetic petrology
675 and rock magnetism of hemo-ilmenite- and magnetite-rich cumulates from the Sokndal Region,
676 South Rogaland, Norway. American Mineralogist, 86, 1447-1468.
677 McEnroe, S.A., Harrison, R.J., Robinson, P., Golla, U. and Jercinovic, M.J. (2001b) The effect of
678 fine-scale microstructures in titanohematite on the acquisition and stability of NRM in granulite
679 facies metamorphic rocks from southwest Sweden: Implications for crustal magnetism. Journal
680 of Geophysical Research, 106, 30523-30546.
681 McEnroe, S.A., Harrison, R.J., Robinson P. and Langenhorst, F. (2002) Nanoscale haematite-
682 ilmenite lamellae in massive ilmenite rock: an example of 'lamellar magnetism' with
683 implications for planetary magnetic anomalies. Geophysical Journal International, 151, 890-
684 912.
685 McEnroe, S.A., Carter-Stiglitz, B., Harrison, R.J., Robinson, P., Fabian, K. and McCammon, C.
686 (2007a) Magnetic exchange bias of more than 1 Tesla in a natural mineral intergrowth. Nature
687 Nanotechnology 2, 631-634.
688 McEnroe, S.A., Robinson, P., Langenhorst, F., Frandsen, C., Terry, M.P., and Boffa Ballaran,T.
689 (2007b) Magnetization of exsolution intergrowths of hematite and ilmenite: Mineral chemistry,
690 phase relations, and magnetic properties of hemo-ilmenite ores with micron- to nanometer-

scale lamellae from Allard Lake, Quebec. Journal of Geophysical Research, 112, B10103, doi:10.1029/2007JB004973.

McEnroe, S. A., Brown, L. L. and Robinson, P. (2008) Remanent and induced magnetic anomalies over a layered intrusion: Effects from crystal fractionation and recharge events. Tectonophysics, 478 119–134. doi: 10.1016/j.tecto.2008.11.021.

McEnroe, S.A., Fabian, K. Robinson, P., Gaina, C. and Brown, L.L. (2009a) Crustal magnetism, lamellar magnetism and rocks that remember. Elements 5, 241-246.

Morrish, A.H. (1994) Canted antiferromagnetism: hematite. World Scientific Publishing, Singapore.

Pouchou, J-L and Pichoir, F. (1984) A new model for quantitative X-ray microanalysis. Part 1. Application to the analysis of homogeneous samples. La Recherche Aerospatiale, 3, 167-192 (in French).

Robinson P., R.J. Harrison, S.A. McEnroe and Hargraves, R. (2002) Lamellar magnetism in the hematite-ilmenite series as an explanation for strong remanent magnetization, Nature, 418, 517-520.

Robinson, P., Harrison, R.J., McEnroe, S.A. and Hargraves, R.G. (2004) Nature and origin of lamellar magnetism in the hematite-ilmenite series. American Mineralogist, 89,725-747.

Robinson, P., Heidelbach, F., Hirt, A.M., McEnroe, S.A. and Brown, L.L. (2006) Crystallographic-magnetic correlations in single crystal haemo-ilmenite: New evidence for lamellar magnetism. Geophysical Journal International, 165, 17-31.

Robinson, P., Fabian, K., and McEnroe, S.A. (2010) The geometry of ionic arrangements and magnetic interactions in ordered ferri-ilmenite solid solutions and its effect on low-temperature magnetic behavior. Geochemistry, Geophysics, Geosystems, 11, Q05Z17, doi:10.1029/2009GC002858.

Robinson, P., Fabian, K., McEnroe, S.A. and Heidelbach, F. (2013) Influence of lattice-preferred orientation with respect to magnetizing field on intensity of remanent magnetization in

polycrystalline hemo-ilmenite. Geophysical Journal International, 192, 514-536. doi: 10.1111/j.1365-246X.2012.05692.x

Toby, B. H. (2001) EXPGUI, a graphical user interface for GSAS. Journal of Applied Crystallography, 34, 210-221.

Van Cappellen, E. & Doukhan, J.-C. (1994. Quantitative X-ray microanalysis of ionic compounds, Ultramicroscopy, **53,** 343–349.

Wechsler, B.A. and Prewitt, C.T. (1984) Crystal structure of ilmenite ($FeTiO_3$) at high temperature and at high pressure. American Mineralogist, 69, 176-185.

Ziff, R.M. and Gu, H. (2009) Universal condition for critical percolation thresholds of kagome-like lattices. Physical. Review E **79** 020102-1 – 020102-4.

Figure Captions

Figure 1 Helicopter aeromagnetic survey map over the Mesoproterozoic basement of the Modum district, south Norway, and the adjacent Permian Oslo Rift to the southeast, with a distinctive ring dike magnetic anomaly (Lutro and Nordgulen 2004). Shows the location of sample MOD-24 and other samples of magnetic interest. The selected area with magnetic color scale and shading was compiled by Giulio Viola from a larger magnetic anomaly map at the Geological Survey of Norway. Side color scale gives magnetic intensities in n T. Red-lavender indicates areas of positive induced magnetization to over 900 nT. Orange through blue indicates areas of negative remanent magnetization, or induced magnetic lows marginal to highs, with values to below -700 n T. Inset map shows geographic location in south Norway. Thin black line indicates the western boundary of the Oslo Rift, which is locally either a normal fault or an unconformity. The positive anomaly southeast of the line in the middle of the figure is caused by gabbros in Mesoproterozoic basement extending southeast beneath the unconformity.

Figure 2 (a) High-resolution reflected-light photomicrograph of polished sample. Hematite host is light-gray. Black spinel lamellae are parallel to (001) of the host. Dark gray blades or rods of rutile are at angles of 60^{o} or greater to the spinel. Very thin gray lamellae parallel to (001) of the host

742 have been identified as ferroan-geikielite. (b) Close-up reflected-light image of spinel and tiny
743 ferroan geikelite plates parallel to (001) of the titanohematite host and blades or rods of rutile
744 formed as attachments to the spinel plates.

745 **Figure 3** Plot of EMP and TEM analyses. Vertical axis is 2Ti /(2Ti+ R^{3+}), providing the total
746 fraction of "ilmenite-like" component, or, inversely, the hematite component. Horizontal axis Mg
747 /[(R^{2+})+ (R^{3+}/2)] gives the absolute value of the $MgTiO_3$ giekielite end member component. EMP
748 trend of Mg-rich titanohematite analyses extrapolates toward a geikielite 0.90 composition.
749 Geikielite TEM analyses are more scattered due to analytical difficulties, but center at geikielite
750 0.70, controlling the TEM Tie Line. Outline shows composition range of Figure 4.

751 **Figure 4** Analyses in the hematite-rich part of Figure 4, extending to "ilm" 0.2 and "geikielite" 0.2
752 (see text for discussion). Analyses of vein hematite of Figure 5 are plotted with exaggerated scale
753 in the extreme hematite-rich corner of the diagram, extending to "ilmenite" 0.01, geikielite 0.01.
754 Maximum "ilmenite" component of any vein hematite is 0.002.

755 **Figure 5** EBS image showing a small part of a clean cross-cutting secondary vein of Ti-free
756 hematite about 200 μm thick, lined with plates of magnesian chlorite parallel to (001) of the host
757 titanohematite.

758 **Figure 6** Bright-field TEM image of a spinel blade and two rutile blades within host titanohematite.
759 The rutile blade to the right appears to show a typical knee of rutile. However, extended study
760 shows that the two orientations are rutile blades lying within two lattice planes of hematite parallel
761 to ***c*** and at angles of ~69° to ***a2*** of hematite. The apparent angles in the foil measured against ***a2*** in
762 Figure 7 are 68° (to left) and 73° (to right) indicating the TEM foil is not tipped exactly parallel to
763 ***a2***.

764 **Figure 7** Selected area electron diffraction patterns of titanohematite (left) and rutile (right) are
765 shown in an orientation such that directions are identical. The zone axis for titanohematite is [211],
766 the one for rutile is [0 -1 1]. The hematite ***a2*** axis for measuring interface angles is [-1 2 0]*.

Figure 8 Lattice orientations of rutile and titanohematite as determined from the selected area diffraction patterns in Figures 6 and 7.

Figure 9 High-resolution TEM image of the interface between titanohematite and rutile. The image is taken in the orientation as shown in Figs. 6 and 7. The trace of the rutile-hematite interface in this view lies at 75° to ***a2*** of hematite (see text discussion) , also rutile interface to the right in Figure 6), and is also inclined at a high angle to the image plane. The lattice planes in rutile are not at 90° to each other, as required by tetragonal symmetry, but at 92°, resulting from sinistral shear (in this view) caused by stretching of rutile along its interface with hematite (see text).

Figure 10 The orientation of a spinel lamella (green) parallel to titanohematite (001) in relation to the approximate plane of the TEM foil (magenta) of Figure 6. Here, the foil is positioned about 32° (rotated approximately about ***a2*** of hematite) and shows the trace of the spinel lamella (shaded green) in the plane of the foil. The foil is in good position to look along the zones axes in Figure 7. The foil could not be rotated enough to bring the hematite ***c***-axis parallel to the beam.

Figure 11 (a) View of titanohematite (black) and rutile (red) dimensional cells looking down ***c*** of titanohematite. This shows the common titanohematite-rutile dimensional best-fit prism plane (purple) at 69° to $\boldsymbol{a_2}$ (x). Note that a minimum strain position requires no rotation about ***c***. A 2° rotation of rutile about ***a1*** (as in Figure 11 c,d) is not sufficient to cause significant change of rutile dimensions in this view. (b) Similar relations in a prism plane (red) 69° from hematite ***a2*** (x) in the opposite direction, used in the cell model of Figure 12a. (c) View of titanohematite (black) and rutile (red) cells within the prism plane in (a). The horizontal cell dimensions (*x'*) are increased in this view compared to the 'true' dimensions, but the vertical dimensions are not. A best-fit line (purple) is achieved in this plane by counterclockwise rotation of the rutile cell by 2° about the common ***a2-a1*** (y) axis. Also shows the orientation of the common lattice plane (blue) changed from 57.63° to 58.9° by the angle of the prism plane. (d) Similar view within the prism plane in (b) with clockwise rotation of the rutile cell. These are the relations shown in Figure 12a.

Figure 12 (a) Three-dimensional array of synthetic rhombohedral cells of titanohematite used to locate a best dimensional fit orientation of elongate rutile blades. Positions of rutile lattice points were tracked numerically. With respect to titanohematite, the dimensional best-fit plane (medium red lines) is parallel to ***c*** (a prism plane) and at an angle of 69° to $\boldsymbol{a_2}$, and the blade long axis (thick red line) is on a best-fit line at an angle of 63° to the titanohematite (001) basal plane. The rutile lattice (not shown here) is rotated 2° clockwise in the best-fit plane to reach the best-fit line. Blue lines show the orientation of the common lattice plane, in this case hematite (102) (see Figure 8). (b) Outline of the same three-dimensional array of titanohematite as in (a) illustrating two possible best-fit planes within the array and two possible best-fit lines in each plane. Arrows indicate the clockwise or counterclockwise directions by which rutile lattices are rotated about the common ***a*** axes (y) to accommodate best-fit. To right (red) is the blade axis modeled in Figure 12a. To left is the actual blade axis (also red) observed in TEM in Figures 6,7,8, with corresponding counterclockwise rotation. In both (a) and (b) anchor points, where titanohematite and rutile lattice points correspond exactly, are at the bottom of the model.

Figure 13 (a) Positions of six prism best-fit planes for rutile in hematite. Each is oriented at an angle of 69° to one of the ***a*** axes. (**b)** Positions of three rutile blades oriented along one best fit line in each of the three planes in (a). Based on the synthetic lattices (Figure 12b), there might be two such lines in each prism plane, thus giving twelve possible orientations. That number could be reduced based on interface details not explored in the simplified model. Also the number of blades visible near given surfaces may be greatly reduced compared to the total number present.

Figure 14 (a) Chemography of the retrograde metamorphic reaction ferri-ilmenite + titanomagnetite = magnetite + rutile as expressed by cation proportions of Fe^{2+}, Fe^{3+}, and Ti^{4+}. **(b)** Chemography similar to Figure 14a in a wider chemical system, with Mg, Zn, and Ni added to the Fe^{2+} apex, and Al, V^{3+} and Cr added to the Fe^{3+} apex, allowing consideration of the reaction aluminous magnesian titanohematite = magnesian spinel + ferrian rutile + Al-poor magnesian titanohematite.

Figure 15 Derived compositions (omitting V_2O_3) in a rhombohedral oxide tetrahedron providing insights into the exsolution sequence during cooling of original aluminous magnesian titanohematite from peak amphibolite-facies conditions to the final intergrowth of magnesian spinel, ferrian rutile, and ferroan geikielite in a magnesian titanohematite host.

Figure 16 $M_s(T)$ and $M_{rs}(T)$ from a MOD-24 sample providing evidence for the Néel temperature of the titanohematite host. There is a clear magnetic phase transition at 600°C (873 K) coincident with the onset of acquisition of remanent magnetization.

Figure 17 Magnetic hysteresis measurements used to identify material behavior. No paramagnetic correction was made. **(a)** Hysteresis loop measured at 300 K (room *T*). The loop is symmetric and indicates a single ferromagnetic material with relatively weak coercivity. (**b)** Hysteresis loop measured on the same sample at 10 K. There is a significant negative hysteresis shift of -40 mT which is similar in character to negative shifts observed at very low T in other samples where there is magnetic interaction across interfaces between titanohematite and ilmenite lamellae. The bulk coercivity (290 mT) is large, and the loop remains open to nearly 1.1T. Shaded profiles show hysteresis differences. Both measurements were made in a maximum field of 1.5 T.

Figure 18 Results of a warming experiment measured in zero field after cooling in a field of 1.5 T to 8 K. With warming from 8 K, the curve shows an initial steep drop in magnetization up to 20-25 K. Above 25 K the negative exchange bias shown in Figure 17b is no longer evident. The plateau edge at ~40 K corresponds in other samples to the conditions where ilmenite magnetization starts to decline during warming.

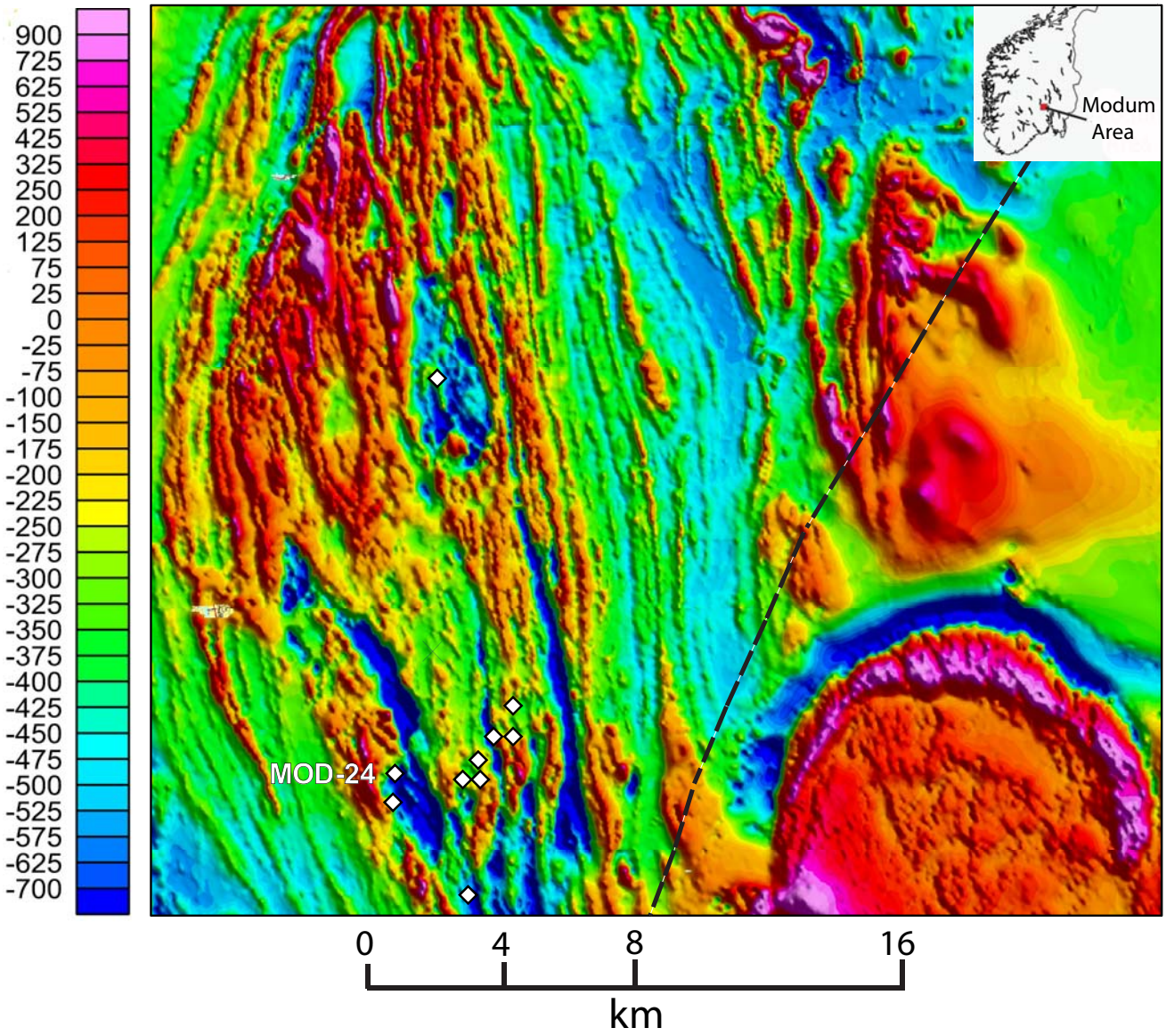
900
725
625
525
425
325
250
200
125
75
25
0
-25
-75
-100
-150
-175
-200
-225
-250
-275
-300
-325
-350
-375
-400
-425
-450
-475
-500
-525
-575
-625
-700
MOD-24
Modum
Area
0
4
8
16
km

Fig. 1

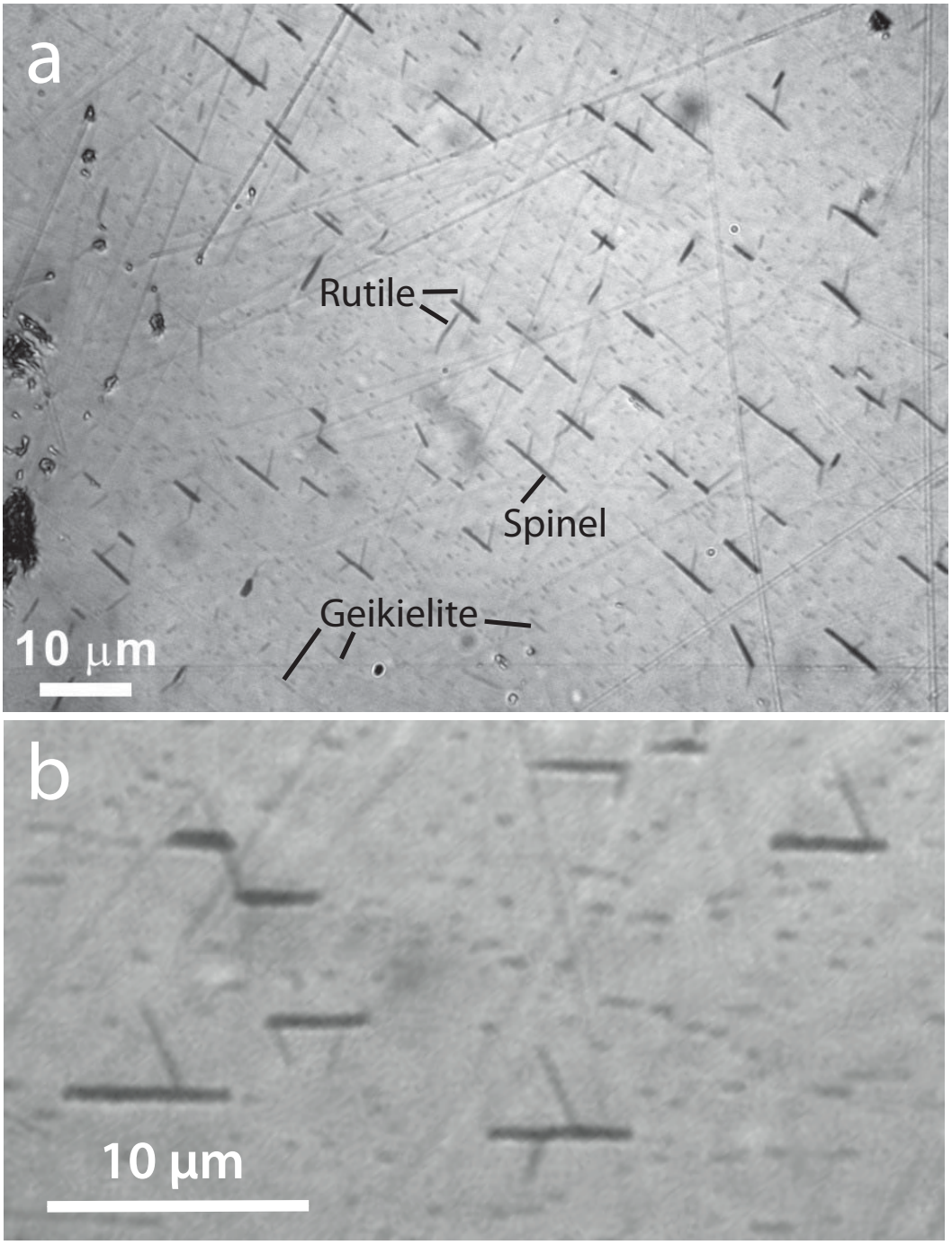

Fig. 2

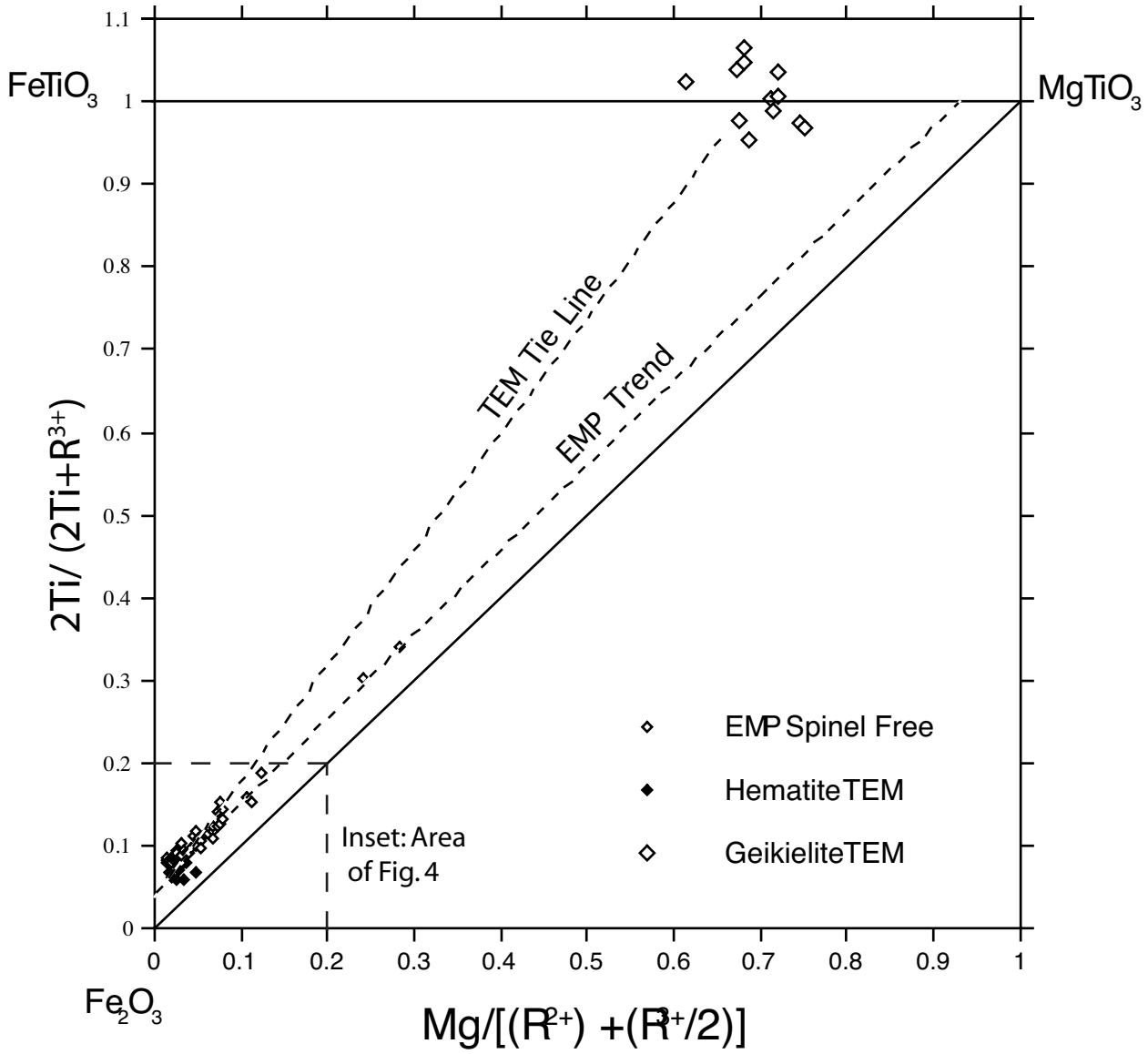
FeTiO3
MgTiO3
Fe2O3
2Ti/ (2Ti+R3+)
Mg/[(R2+) +(R3+/2)]
TEM Tie Line
EMP Trend
Inset: Area of Fig. 4
EMP Spinel Free
HematiteTEM
GeikieliteTEM
0
0.1
0.2
0.3
0.4
0.5
0.6
0.7
0.8
0.9
1
1.1

Fig. 3

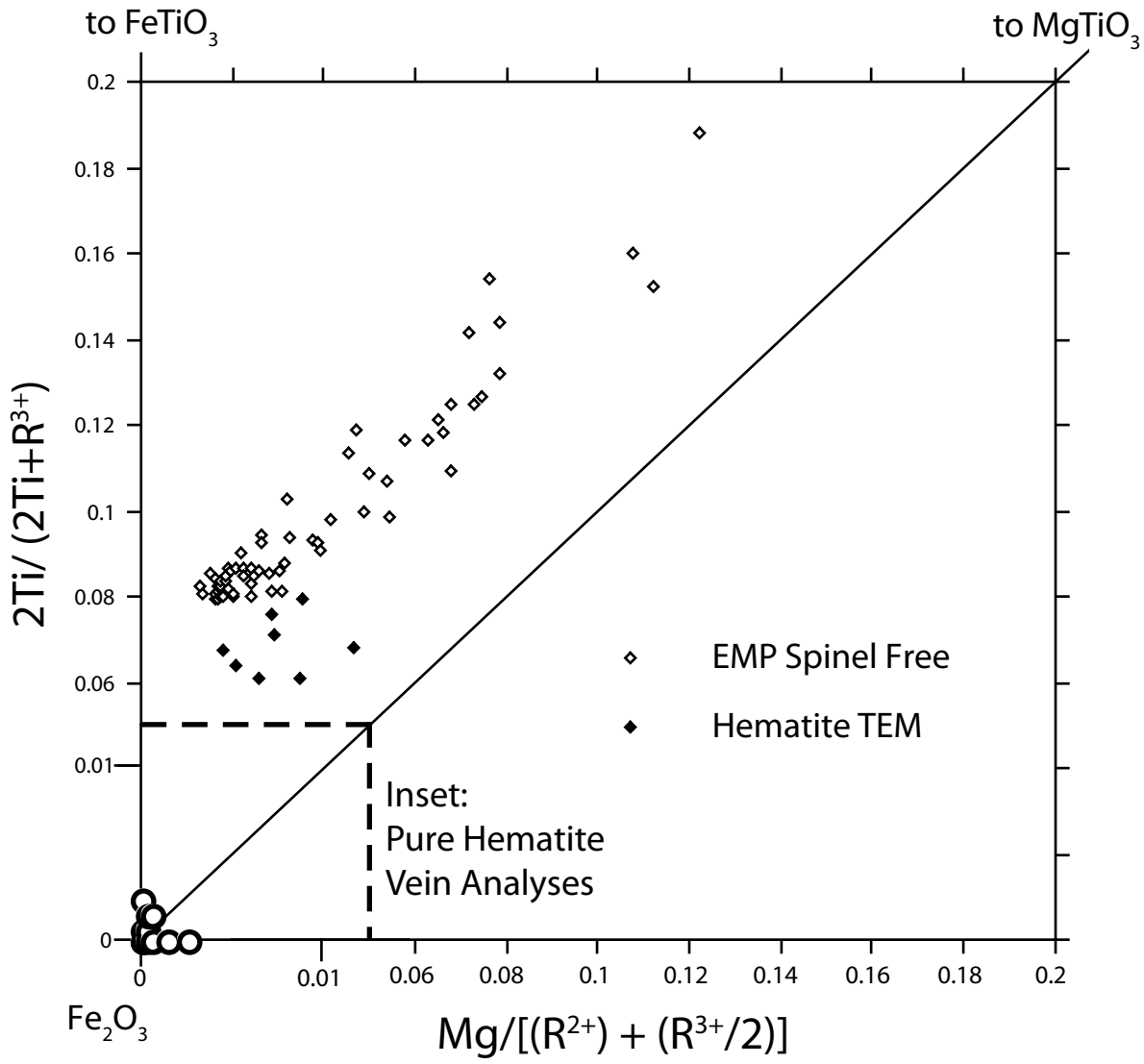
to FeTiO3
to MgTiO3
2Ti/ (2Ti+R3+)
Mg/[(R2+) + (R3+/2)]
Fe2O3
EMP Spinel Free
Hematite TEM
Inset:
Pure Hematite
Vein Analyses
0
0.01
0.06
0.08
0.1
0.12
0.14
0.16
0.18
0.2

Fig. 4

Fig. 5

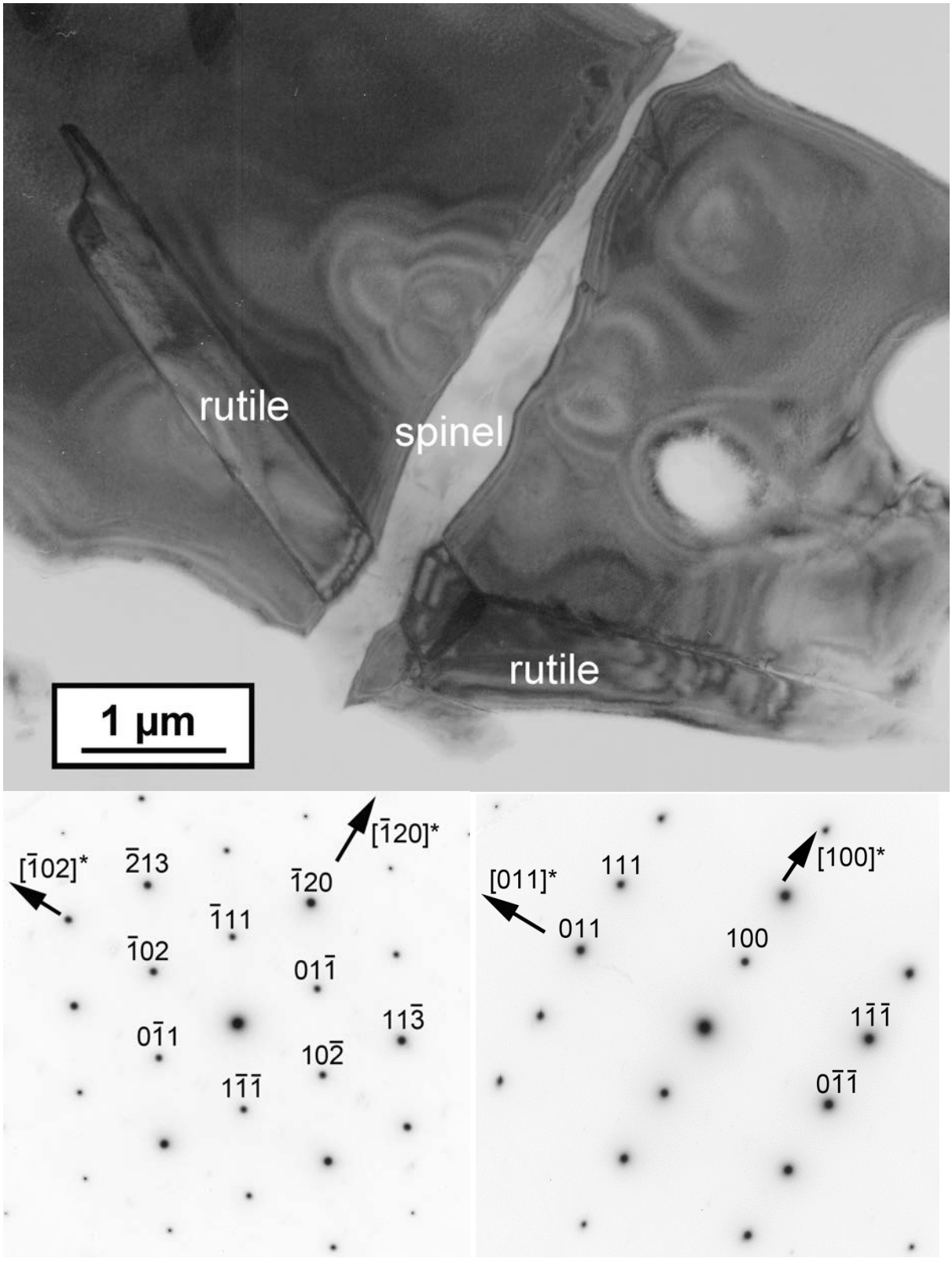
rutile
spinel
rutile
1 µm
[$\bar{1}$02]*
$\bar{2}$13
[$\bar{1}$20]*
$\bar{1}$20
$\bar{1}$11
$\bar{1}$02
01$\bar{1}$
0$\bar{1}$1
11$\bar{3}$
10$\bar{2}$
1$\bar{1}\bar{1}$
[011]*
111
[100]*
011
100
1$\bar{1}\bar{1}$
0$\bar{1}\bar{1}$

Figs. 6, 7

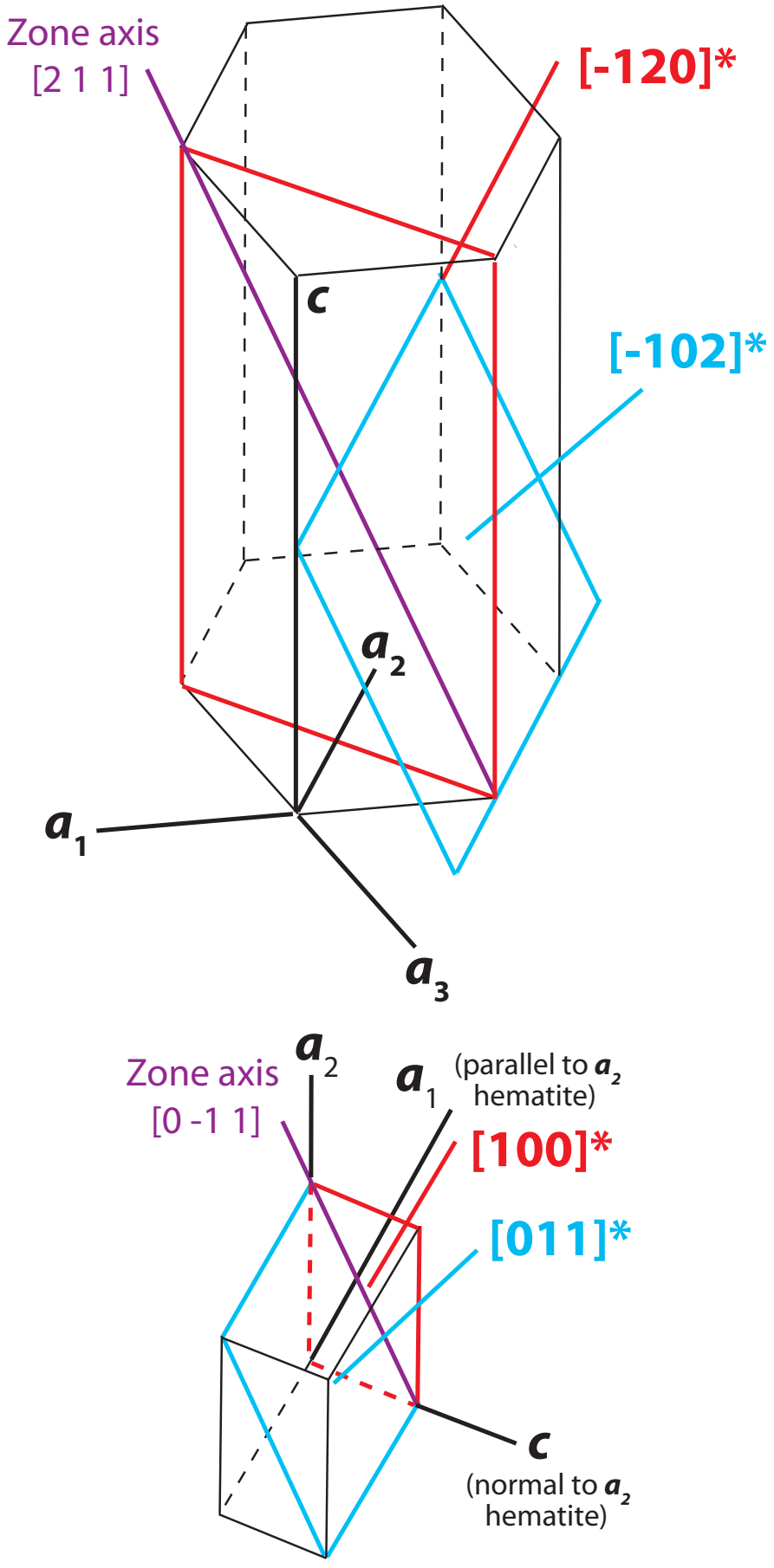
Zone axis
[2 1 1]
[-120]*
c
[-102]*
a2
a1
a3
a2
Zone axis
[0 -1 1]
a1
(parallel to a2
hematite)
[100]*
[011]*
c
(normal to a2
hematite)

Fig. 8

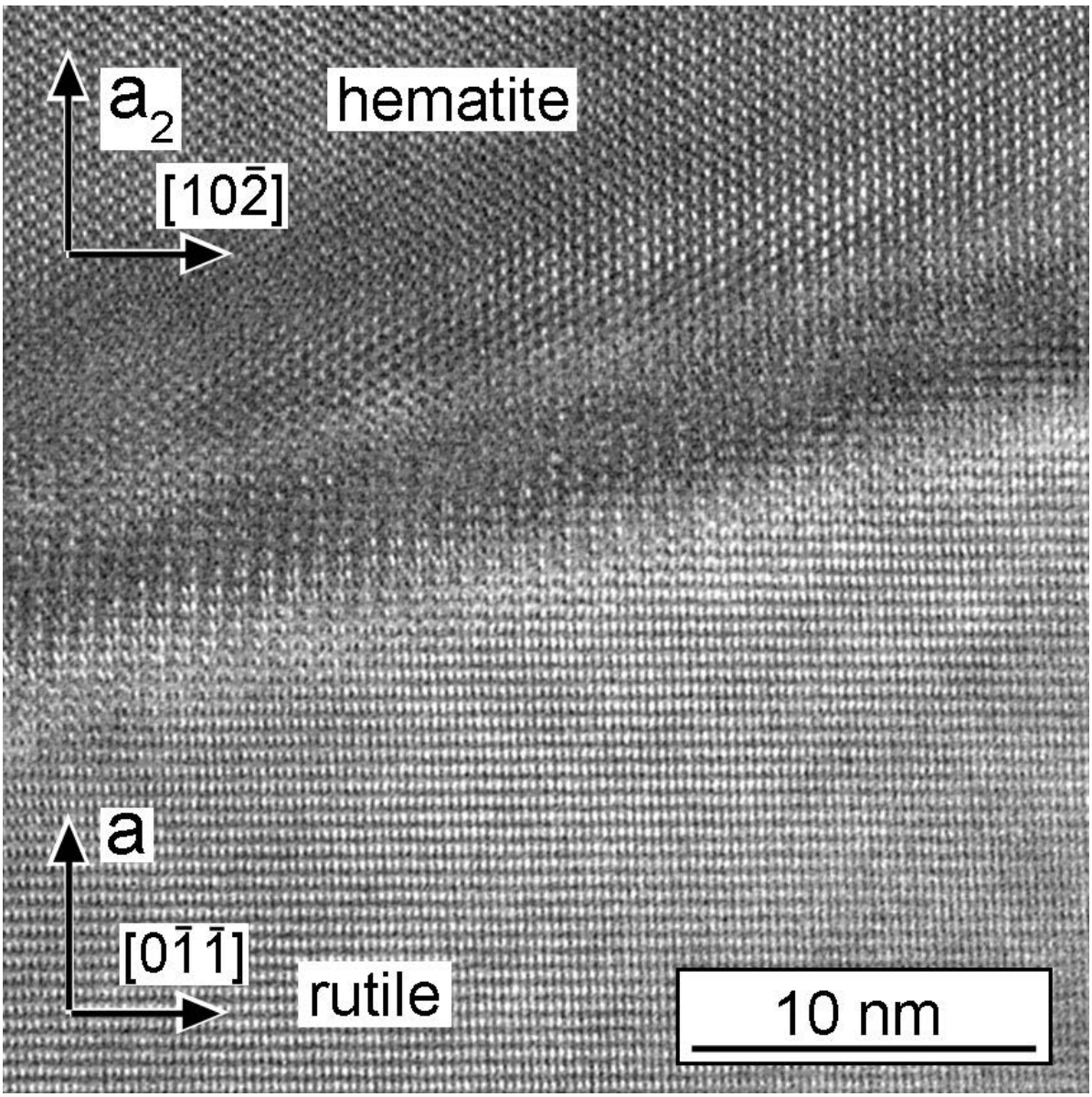

Fig. 9

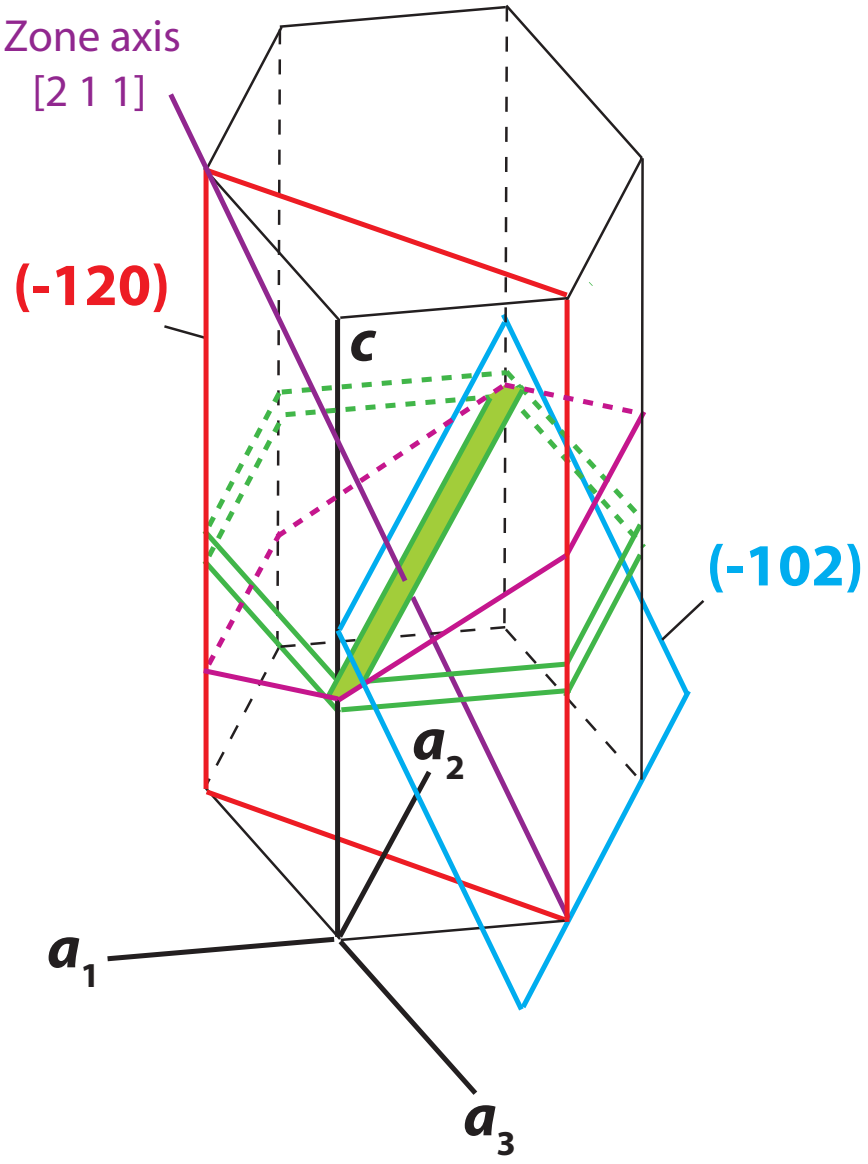

Fig. 10

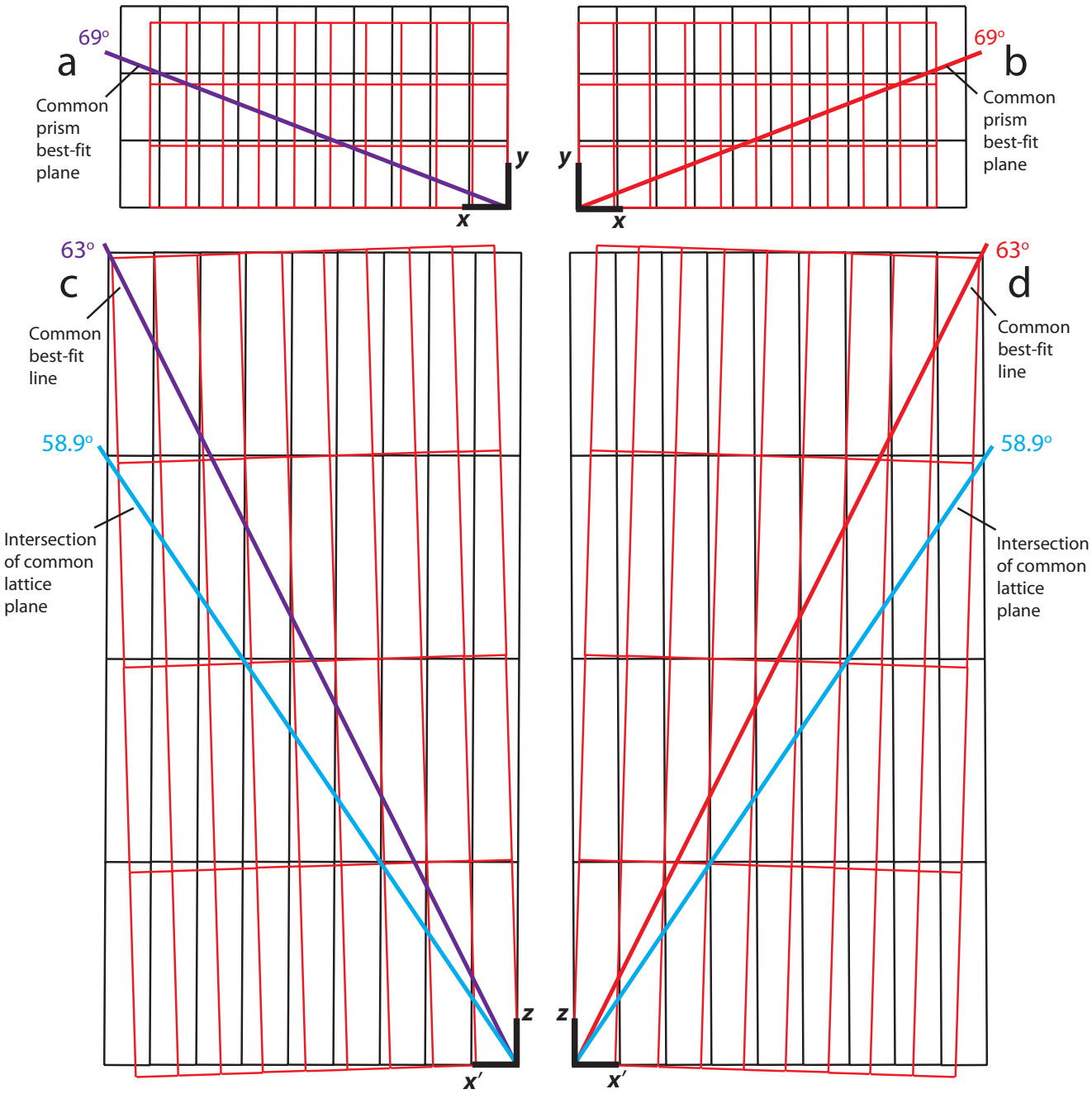
69°
a
Common prism best-fit plane
y
x
69°
b
Common prism best-fit plane
y
x
63°
c
Common best-fit line
58.9°
Intersection of common lattice plane
z
x′
63°
d
Common best-fit line
58.9°
Intersection of common lattice plane
z
x′

Fig. 11

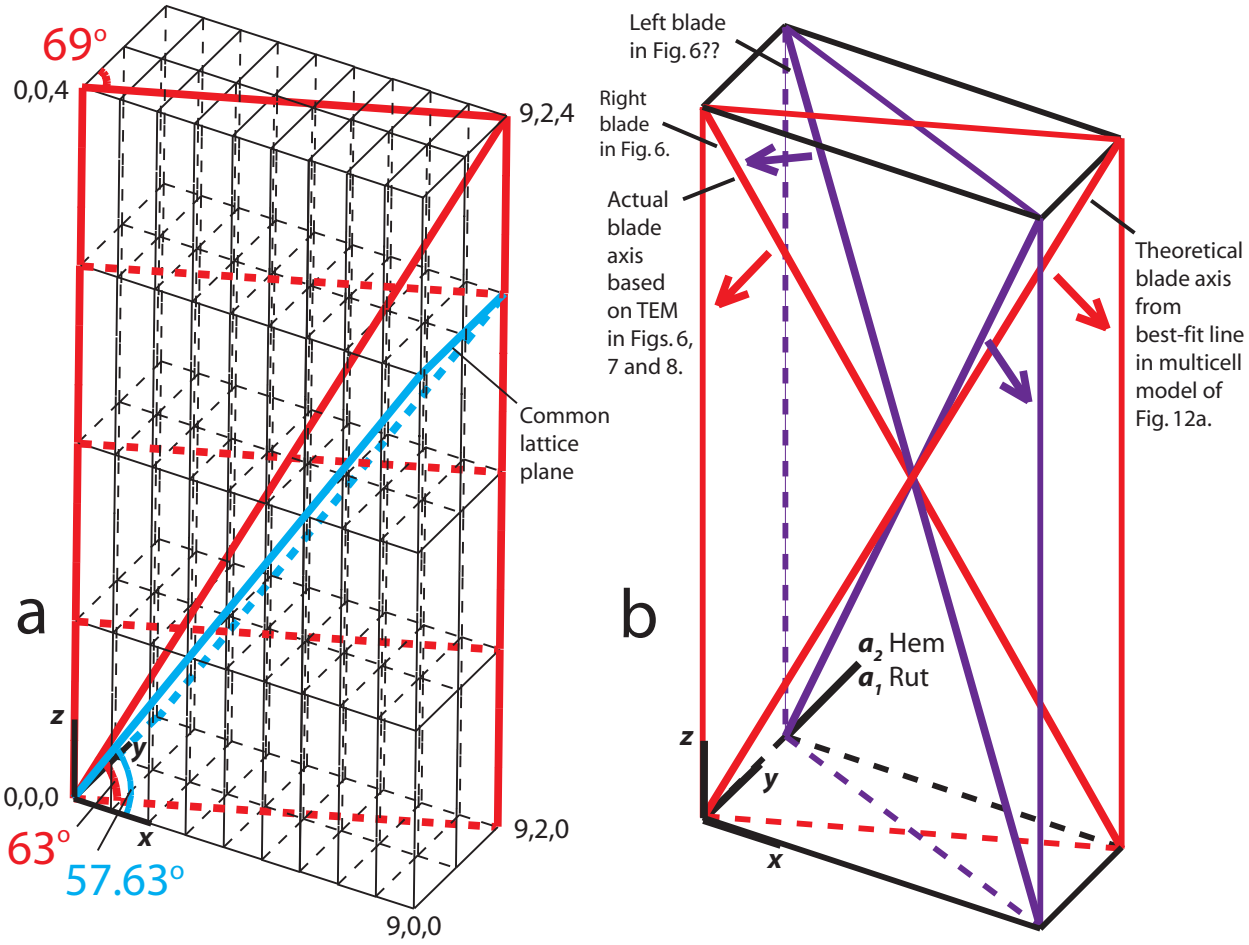
69°
0,0,4
9,2,4
Common lattice plane
a
z
y
0,0,0
63°
x
57.63°
9,2,0
9,0,0
Left blade in Fig. 6??
Right blade in Fig. 6.
Actual blade axis based on TEM in Figs. 6, 7 and 8.
Theoretical blade axis from best-fit line in multicell model of Fig. 12a.
b
a_2 Hem
a_1 Rut
z
y
x

Fig. 12

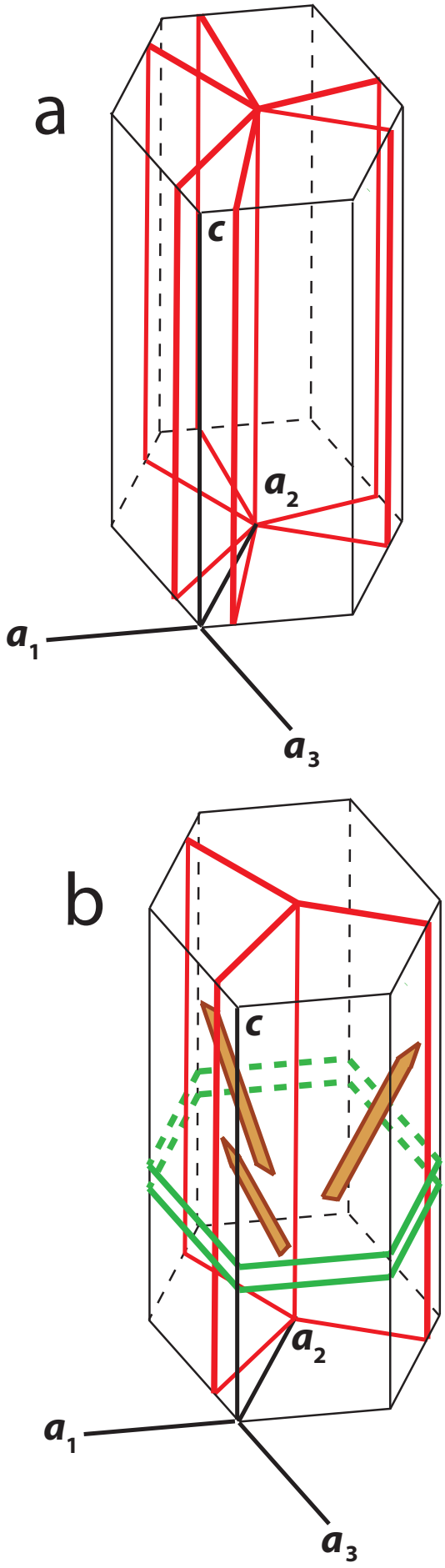

Fig. 13

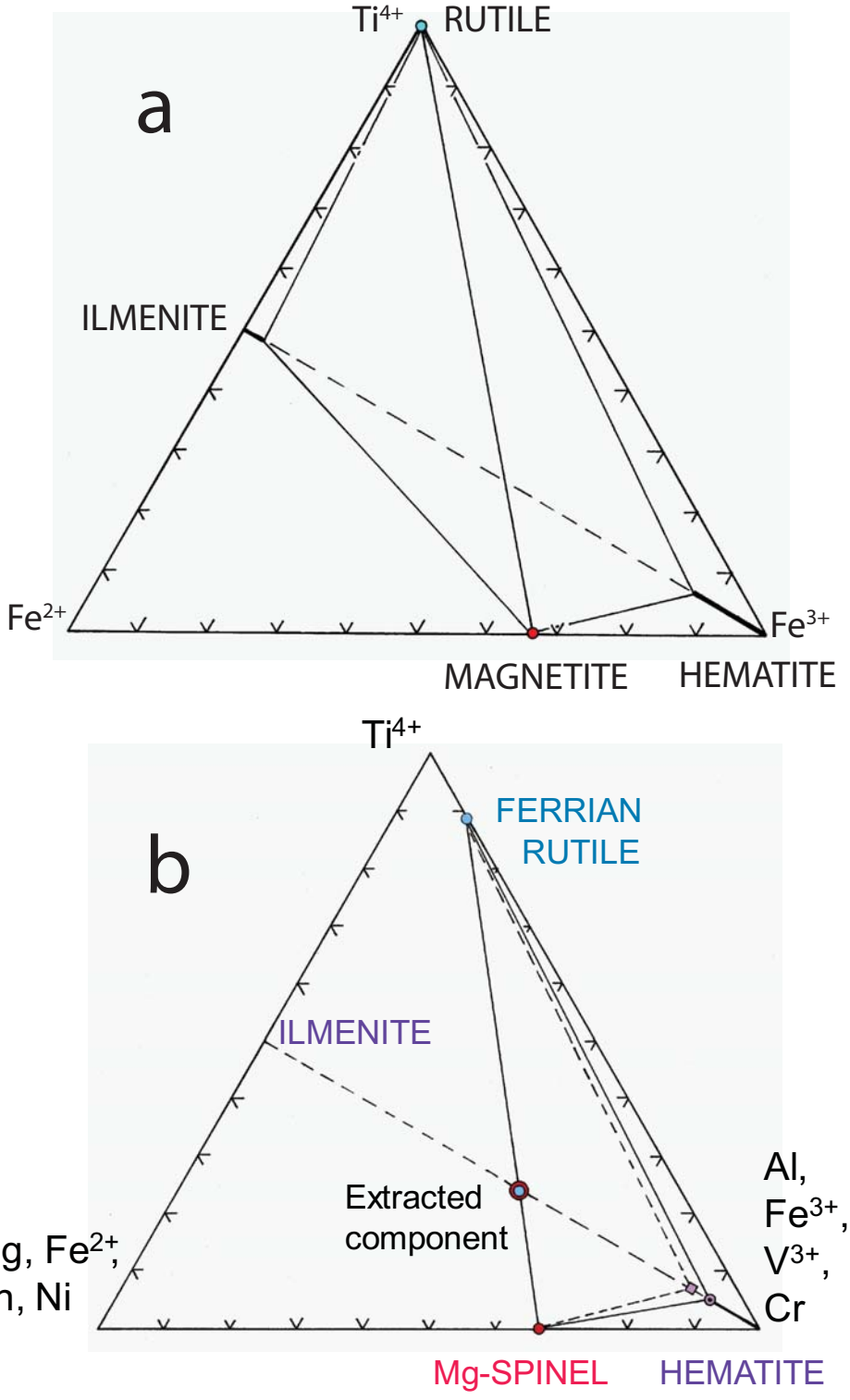
a
Ti4+
RUTILE
ILMENITE
Fe2+
Fe3+
MAGNETITE
HEMATITE
b
Ti4+
FERRIAN
RUTILE
ILMENITE
Extracted
component
Mg, Fe2+,
Zn, Ni
Al,
Fe3+,
V3+,
Cr
Mg-SPINEL
HEMATITE

Fig. 14

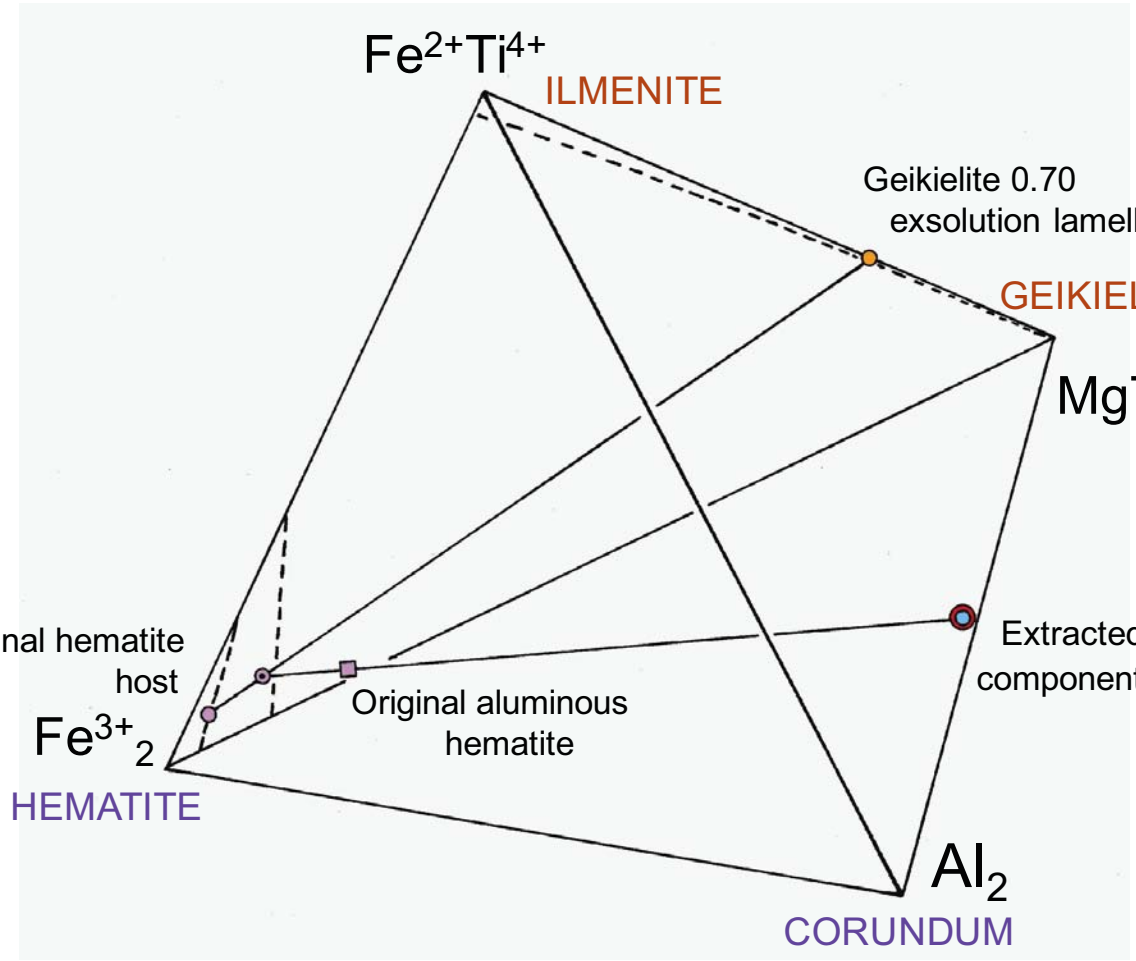
$Fe^{2+}Ti^{4+}$
ILMENITE
Geikielite 0.70
exsolution lamellae
GEIKIELITE
$MgTi^{4+}$
Final hematite
host
Fe^{3+}_2
HEMATITE
Original aluminous
hematite
Extracted
component
Al_2
CORUNDUM

Fig. 15

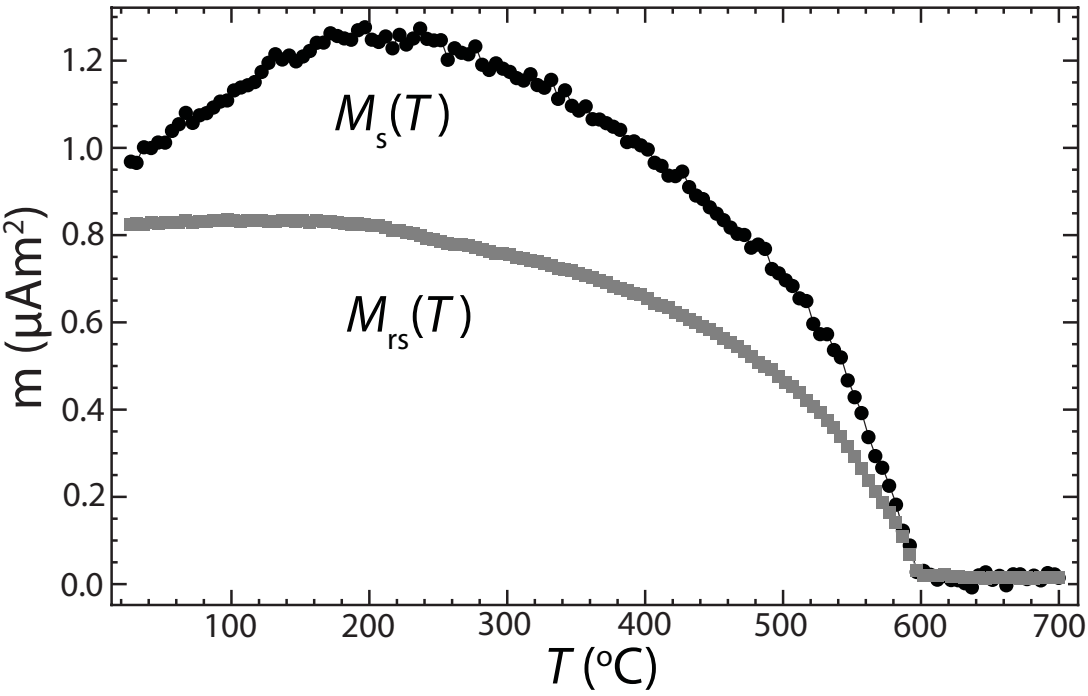

Fig. 16

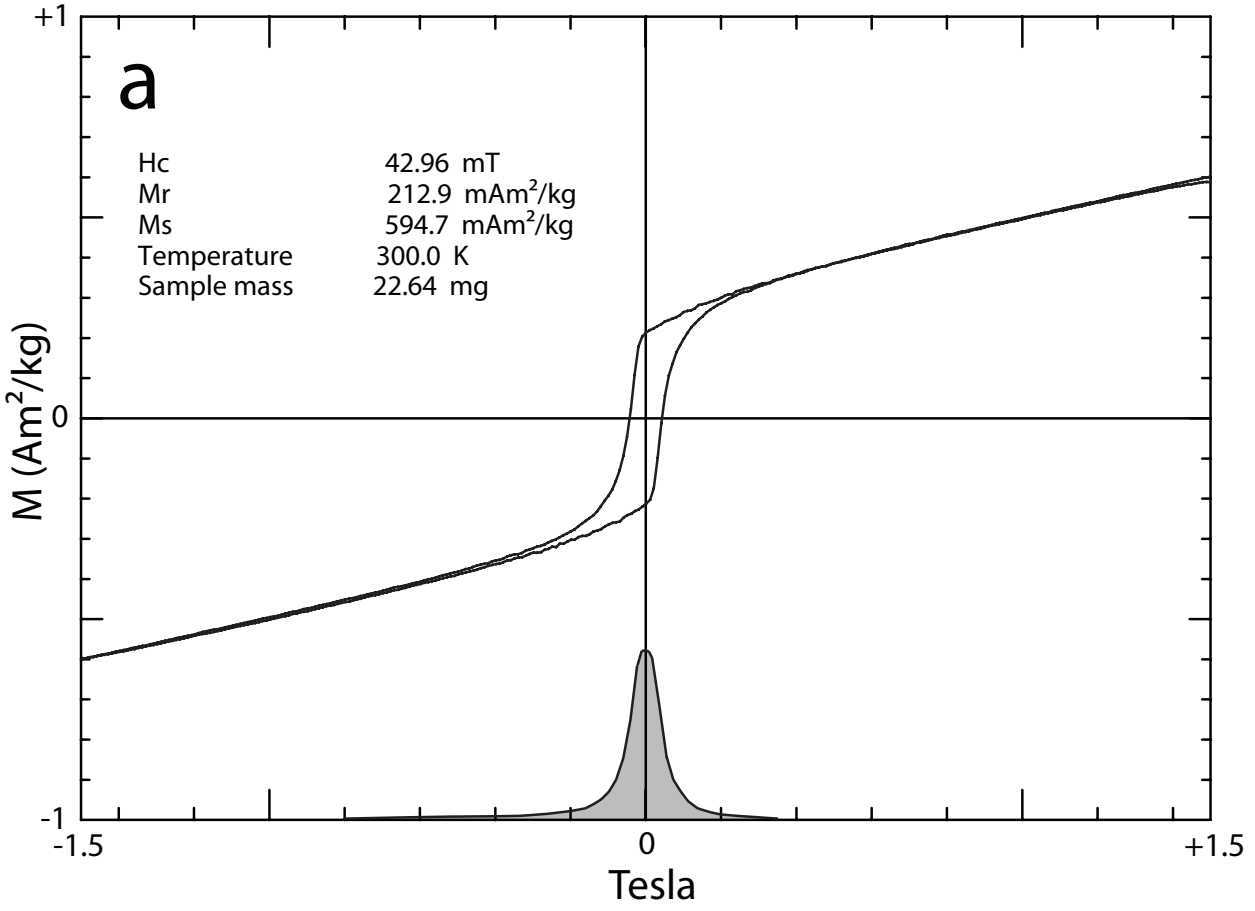
a
Hc 42.96 mT
Mr 212.9 mAm²/kg
Ms 594.7 mAm²/kg
Temperature 300.0 K
Sample mass 22.64 mg
M (Am²/kg)
+1
0
-1
-1.5
0
+1.5
Tesla

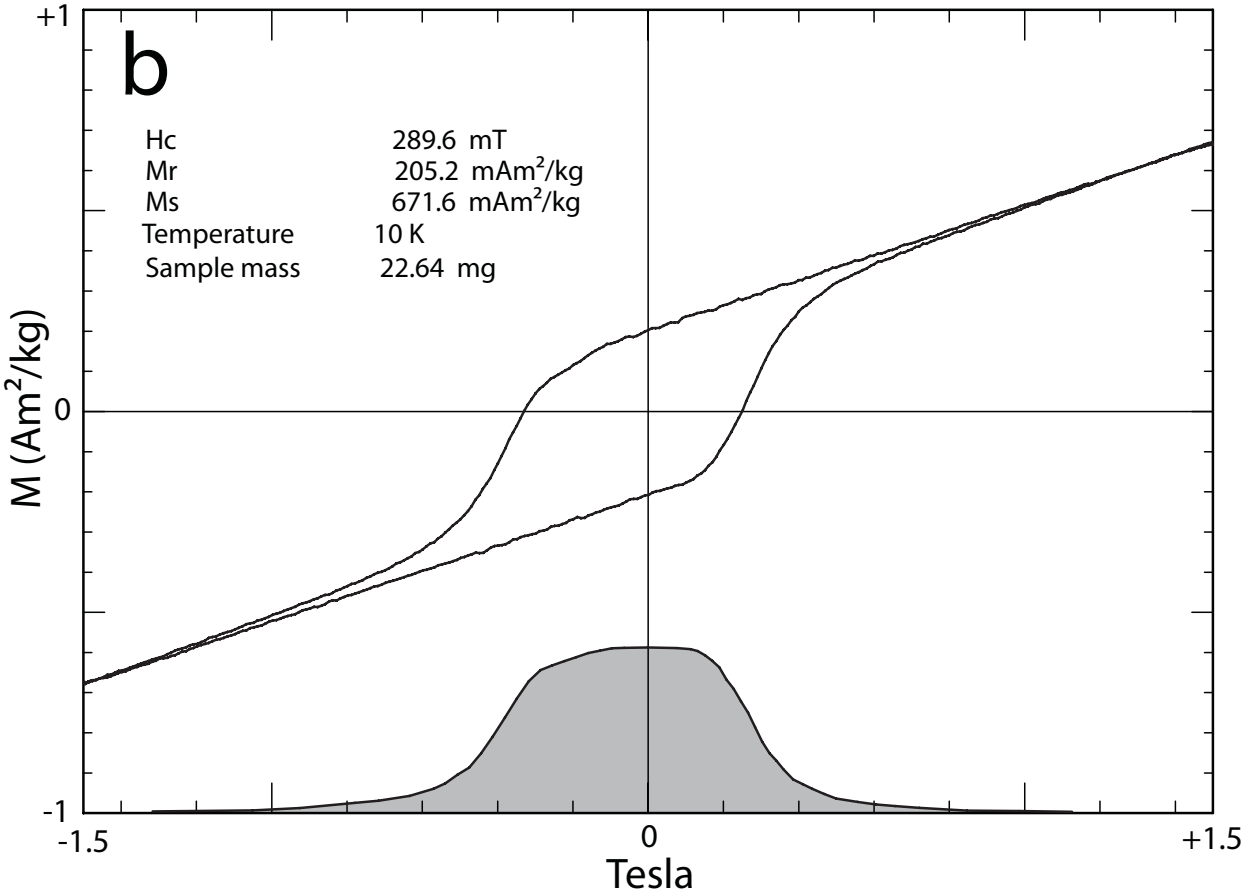
b
Hc 289.6 mT
Mr 205.2 mAm²/kg
Ms 671.6 mAm²/kg
Temperature 10 K
Sample mass 22.64 mg
M (Am²/kg)
+1
0
-1
-1.5
0
+1.5
Tesla

Fig. 17

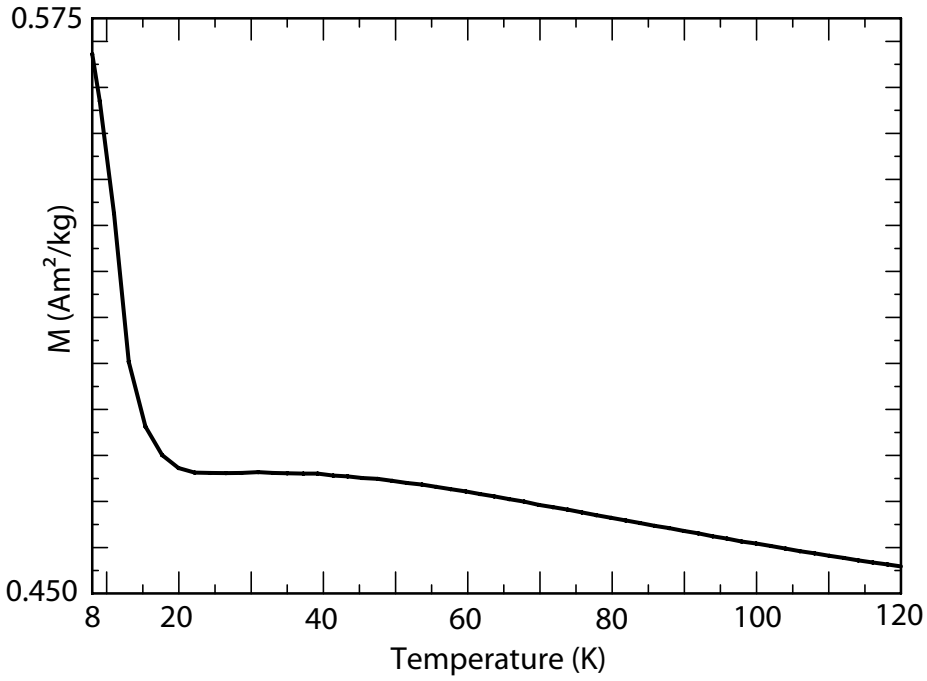

Fig. 18

Table 1. EMP analyses, cation formulae, and end-member percentages of spinel (left) and rutile (right).

	Point	1	2	3	4
	Nb2O5 a	*0.019*	*0.007*	*0.032*	*0.019*
	SiO2		*0.02*	*0.005*	*0.025*
	TiO2	0.115	0.113	0.174	0.137
Wt.%	Al2O3	69.515	69.743	69.501	69.473
Oxides	Cr2O3	0.156	0.172	0.104	0.106
	V2O3	0.025	0.008	0.016	0.022
	Fe Tot (FeO)	4.266	4.403	4.186	4.462
	MnO	*0.028*	*0.002*		
	MgO	28.111	28.154	28.157	28.298
	ZnO	*0.028*	*0.056*	*0.045*	
	NiO	*0.059*	*0.058*	*0.029*	*0.052*
	Total	b 102,322	102.736	102.249	102.594
	Si	0.0000	0.0005	0.0001	0.0006
	Ti	0.0020	0.0020	0.0031	0.0024
	Al	1.9244	1.9238	1.9248	1.9181
	Cr	0.0029	0.0032	0.0019	0.0020
	V	0.0005	0.0002	0.0003	0.0004
Cats/3	Fe3+	0.0681	0.0680	0.0666	0.0735
	Mg	0.9842	0.9821	0.9862	0.9881
	Ni	0.0011	0.0011	0.0005	0.0010
	Fe2+	0.0157	0.0182	0.0157	0.0139
	Mn	0.0006	0.0000	0.0000	0.0000
	Zn	0.0005	0.0010	0.0008	0.0000
	Sum	3.0000	3.0000	3.0000	3.0000
	Ox/3Cats	3.9659	3.9660	3.9667	3.9633
	4-Ox	0.0341	0.0340	0.0333	0.0367
	Fe3+	0.0681	0.0680	0.0666	0.0735
	Fe2+	0.0157	0.0182	0.0157	0.0139
	Fe3+/FeTot	0.8129	0.7886	0.8094	0.8407
	Fe2SiO4	0.0000	0.0468	0.0117	0.0586
	Fe2TiO4	**0.2031**	**0.1989**	**0.3075**	**0.2414**
Percentages	FeCr2O4	0.1449	0.1591	0.0966	0.0982
of End	FeV2O4	0.0235	0.0075	0.0151	0.0207
Members	**FeFe2O4**	**3.4061**	**3.3982**	**3.3291**	**3.6744**
	Sum	3.7776	3.8105	3.7600	4.0931
	MgAl2O4	**98.4195**	**98.2142**	**98.6184**	**98.8090**
	FeAl2O4 c	-2.4128	-2.2346	-2.5113	-3.0001
	NiAl2O4	0.1115	0.1092	0.0548	0.0980
	MnAl2O4	0.0557	0.0040	0.0000	0.0000
	ZnAl2O4	0.0486	0.0968	0.0781	0.0000
	Sum	96.2224	96.1895	96.2400	95.9069
	Total	100.0000	100.0000	100.0000	100.0000

Note: Wt% values in italics are below MDL (see Table 1A)
a Analyzed Nb2O5 not used in analytical sums nor formulations.
b Extremely high analytical sums for spinels seem to be quite routine in several laboratories, This is probably related to Al standardization, but the exact cause is not known.

	Point	7	6
	SiO2	0.022	0.04
	TiO2	81.288	80.486
	Al2O3		0.032
Wt.% Oxides	Fe2O3	15.954	15.219
	Fe Tot (FeO)	14.356	13.694
	MnO	0.032	0.047
	MgO	0.248	0.218
	ZnO	0.029	0.097
	Ta2O5	0.078	0.004
	V2O3	2.207	2.205
	Total	98.26	96.823
	Corr.Total	99.858	98.348
	Si	0.0003	0.0006
	Ti	0.8814	0.8831
	Al	0.0000	0.0006
	V	0.0255	0.0258
Cats/1	Fe3+	0.0866	0.0836
	Mg	0.0053	0.0047
	Mn	0.0004	0.0006
	Zn	0.0003	0.0010
	Ta	0.0002	0.0000
	Sum	1.0000	1.0000
	Ox/1Cats	1.9380	1.9387
	2-0x	0.0620	0.0613
	H20	0.0620	0.0613
	OH	0.1240	0.1226
	R5+	0.0002	0.0000
Cation	R4+	0.8817	0.8837
Summary	R3+	0.1121	0.1099
	R2+	0.0060	0.0064
	H1+	0.1240	0.1226
	TotalCharge	4.0000	4.0000
	SiO2	0.032	0.058
Percentages	TiO2	88.143	88.315
of End	a MgTaO2	0.023	0.001
Members	Al0(OH)	0.000	0.055
	VO(OH)	2.551	2.580
	Fe3+O(OH)	8.656	8.355
	Mg(OH)2	0.525	0.474
	Mn(OH)2	0.039	0.058
	Zn(OH)2	0.031	0.105
	Sum	100.000	100.000

Note: Wt% analyses in italics are below MDL (see Table 1A). Of four analyses substantially of rutile, only two werefree from effects of overlap with titanohematite. Analysis 6 shows a low analytical sum, but is otherwise similarto the superior analysis 7.

c Negative values indicate not enough R2+ to accomodate Al3+.
Probably consequence of excessive Al2O3.

a Formula Mg 0.333 Ta 0.6667 O2

Table 1A Instrument, instrument conditions and standards for electron probe analyses.

Electron probe micro-analysis (EPMA) was done using the Cameca SX50 at the University of Massachusetts. This is a five wavelength-dispersive spectrometer instrument, automated via Cameca's SXRayN50 software (Sun-Unix platform). Analysis was performed using a 15kV, 20nA focused beam. Count times were 20 seconds for all elements. Corrections for differential matrix effects were done using the PAP routine (Pouchou and Pichoir, 1984). Detection limits were calculated using the method of Ancey (1978). Analyzing monochromators, standards and minimum detectability limits (MDL) are summarized in the table below.

element	line	xtal	Std	Atomic MDL	Oxide MDL
K	Ka	PET	sanidine (P-28)	0.0234	0.0282
Si	Ka	TAP	pg721 (kiglapait labradorite)	0.0208	0.0445
Al	Ka	TAP	albite (P103-Amelia)	0.0315	0.0595
Ti	Ka	PET	tio2 (P530-synthetic)	0.0281	0.0469
V	Ka	PET	V	0.0340	0.0500
Fe	Ka	LIF	fayalite-rockport	0.0917	0.1180
Mn	Ka	LIF	rhodonite AMNH 41522	0.0666	0.0860
Cr	Ka	LIF	52-nl11 (chromite-Stillwater)	0.0546	0.0798
Zn	Ka	LIF	ZnO (P471)	0.1647	0.2050
Ca	Ka	PET	pg721 (kiglapait labradorite)	0.0243	0.0340
S	Ka	PET	Pyrite-MAC	0.0310	
Mg	Ka	TAP	crcats (diopside-synthetic)	0.0706	0.1171
Ni	Ka	LIF	nio (synthetic)	0.0709	0.0902
Nb	La	PET	Nb	0.1282	0.1834
Ta	La	LIF	Ta	0.3308	0.4039

Table 2. EMP analyses of titanohematite, cation formulae, end-member calculations and plotting ratios.

	Traverse	1	1	1	1	1	1	1	1	1	1	1	1	1
	Point	1	2	3	4	6	12	13	14	15	18	24	26	31
	SiO2							*0.009*				*0.006*		*0.026*
	TiO2	4.124	5.6230	3.939	3.872	6.218	4.566	4.049	4.008	5.735	6.299	4.062	4.014	5.845
	Al2O3	0.198	0.1900	0.215	0.243	0.226	0.189	0.186	0.164	0.168	0.168	0.167	0.153	0.232
Wt%	Cr2O3	0.145	0.1430	0.139	0.107	0.161	0.15	0.212	0.185	0.141	0.126	0.111	0.127	0.113
Oxides	V2O3	0.122	0.1480	0.141	0.12	0.175	0.131	0.163	0.143	0.17	0.187	0.144	0.152	0.178
	a Nb2O5	*0.016*				*0.006*	*0.011*		*0.039*			*0.039*		*0.027*
	a Ta2O5	*0.196*	*0.2190*	*0.326*	*0.298*	*0.176*	*0.269*	0.635	*0.204*	0.427	*0.067*	*0.355*	*0.319*	*0.284*
	Fe2O3	92.460	88.9059	92.150	91.102	87.927	90.983	91.896	91.678	89.565	88.112	91.271	91.825	88.876
	Fe Tot (FeO)	86.225	83.0790	85.843	85.042	81.696	84.412	85.715	85.651	83.125	81.644	84.738	85.313	82.403
	FeO	3.028	3.0805	2.926	3.068	2.578	2.545	3.026	3.158	2.533	2.359	2.611	2.687	2.431
	MnO	*0.019*	*0.0420*	*0.042*		*0.016*	*0.033*			*0.012*		*0.042*	*0.004*	*0.021*
	MgO	0.45	1.1630	0.435	0.339	1.736	0.962	0.569	0.329	1.621	1.87	0.717	0.614	1.706
	CaO	*0.003*			*0.003*	*0.008*		*0.019*	*0.027*			*0.001*	*0.016*	*0.006*
	NiO		*0.0030*	*0.011*		*0.014*					*0.016*		*0.011*	
	Total	91.498	90.610	91.091	90.024	90.432	90.723	91.557	90.75	91.399		90.382	90.723	90.841
	Corr.Total	100.762	99.517	100.323	99.151	99.241	99.838	100.764	99.935	100.372	99.205	99.526	99.923	99.745
	Si	0.0000	0.0000	0.0000	0.0000	0.0000	0.0000	0.0002	0.0000	0.0000	0.0000	0.0002	0.0000	0.0007
	Ti	0.0812	0.1113	0.0779	0.0776	0.1227	0.0903	0.0798	0.0796	0.1123	0.1242	0.0809	0.0796	0.1149
	Al	0.0061	0.0059	0.0067	0.0076	0.0070	0.0059	0.0057	0.0051	0.0052	0.0052	0.0052	0.0048	0.0071
Cats/2	Cr	0.0030	0.0030	0.0029	0.0023	0.0033	0.0031	0.0044	0.0039	0.0029	0.0026	0.0023	0.0026	0.0023
	V3+	0.0026	0.0031	0.0030	0.0026	0.0037	0.0028	0.0034	0.0030	0.0035	0.0039	0.0031	0.0032	0.0037
	Nb5+	0.0002	0.0000	0.0000	0.0000	0.0001	0.0001	0.0000	0.0005	0.0000	0.0000	0.0005	0.0000	0.0003
	Ta5+	0.0014	0.0016	0.0023	0.0022	0.0013	0.0019	0.0045	0.0015	0.0030	0.0005	0.0026	0.0023	0.0020
	Fe3+	1.8212	1.7607	1.8246	1.8260	1.7366	1.8014	1.8127	1.8229	1.7548	1.7384	1.8183	1.8232	1.7486
	Fe Tot	1.8875	1.8285	1.8890	1.8943	1.7932	1.8574	1.8791	1.8927	1.8099	1.7902	1.8761	1.8825	1.8017
	Fe2+	0.0663	0.0678	0.0644	0.0683	0.0566	0.0560	0.0663	0.0698	0.0552	0.0517	0.0578	0.0593	0.0532
	Mg	0.0176	0.0456	0.0171	0.0135	0.0679	0.0377	0.0222	0.0130	0.0629	0.0731	0.0283	0.0241	0.0665
	Mn	0.0004	0.0009	0.0009	0.0000	0.0004	0.0007	0.0000	0.0000	0.0003	0.0000	0.0009	0.0001	0.0005
	Ca	0.0001	0.0000	0.0000	0.0001	0.0002	0.0000	0.0005	0.0008	0.0000	0.0000	0.0000	0.0005	0.0002
	Ni	0.0000	0.0001	0.0002	0.0000	0.0003	0.0000	0.0000	0.0000	0.0000	0.0003	0.0000	0.0002	0.0000
	Sum	2.0000	2.0000	2.0000	2.0000	2.0000	2.0000	2.0000	2.0000	2.0000	2.0000	2.0000	2.0000	2.0000
	Sum Fe Tot	2.0000	2.0000	2.0000	2.0000	2.0000	2.0000	2.0000	2.0000	2.0000	2.0000	2.0000	2.0000	2.0000
	Ox/2Cats	2.0894	2.1196	2.0877	2.0870	2.1317	2.0993	2.0936	2.0885	2.1226	2.1308	2.0909	2.0884	2.1257
	3-Ox	0.9106	0.8804	0.9123	0.9130	0.8683	0.9007	0.9064	0.9115	0.8774	0.8692	0.9091	0.9116	0.8743
	Fe3+	1.8212	1.7607	1.8246	1.8260	1.7366	1.8014	1.8127	1.8229	1.7548	1.7384	1.8183	1.8232	1.7486
	Fe2+	0.0663	0.0678	0.0644	0.0683	0.0566	0.0560	0.0663	0.0698	0.0552	0.0517	0.0578	0.0593	0.0532
	Fe3+/FeTot	0.9649	0.9629	0.9659	0.9639	0.9684	0.9699	0.9647	0.9631	0.9695	0.9711	0.9692	0.9685	0.9705
	FeSiO3	0.0000	0.0000	0.0000	0.0000	0.0000	0.0000	0.0236	0.0000	0.0000	0.0000	0.0159	0.0000	0.0680
	b FeNbO3	0.0284	0.0000	0.0000	0.0000	0.0107	0.0196	0.0000	0.0699	0.0000	0.0000	0.0700	0.0000	0.0479
	c FeTaO3	0.2093	0.2351	0.3499	0.3238	0.1884	0.2887	0.6790	0.2199	0.4535	0.0717	0.3834	0.3433	0.3029
	FeTiO3	6.3116	6.4666	5.9713	6.4012	5.3937	5.1882	5.7053	6.5920	4.9116	5.0780	5.1606	5.4724	4.7805
End	MgTiO3	1.7557	4.5621	1.7060	1.3458	6.7911	3.7727	2.2232	1.2958	6.2905	7.3079	2.8293	2.4147	6.6482
Members	MnTiO3	0.0421	0.0936	0.0936	0.0000	0.0356	0.0735	0.0000	0.0000	0.0265	0.0000	0.0942	0.0089	0.0465
	CaTiO3	0.0084	0.0000	0.0000	0.0086	0.0225	0.0000	0.0534	0.0764	0.0000	0.0000	0.0028	0.0452	0.0168
	NiTiO3	0.0000	0.0063	0.0233	0.0000	0.0296	0.0000	0.0000	0.0000	0.0000	0.0337	0.0000	0.0233	0.0000
	Sum	8.3555	11.3638	8.1441	8.0794	12.4715	9.3428	8.6844	8.2540	11.6821	12.4913	8.5562	8.3080	11.9107
	Fe2O3	91.0610	88.0366	91.2293	91.2984	86.8278	90.0700	90.6373	91.1459	87.7376	86.9220	90.9143	91.1609	87.4285
	Cr2O3	0.1500	0.1488	0.1446	0.1127	0.1670	0.1560	0.2197	0.1932	0.1451	0.1306	0.1162	0.1325	0.1168
	V2O3	0.1280	0.1561	0.1487	0.1281	0.1841	0.1382	0.1713	0.1515	0.1774	0.1965	0.1528	0.1608	0.1866
	Al2O3	0.3054	0.2947	0.3334	0.3814	0.3495	0.2930	0.2873	0.2554	0.2578	0.2596	0.2605	0.2379	0.3574
	Sum	91.6445	88.6362	91.8559	91.9206	87.5285	90.6572	91.3156	91.7460	88.3179	87.5087	91.4438	91.6920	88.0893
	Total	100	100	100	100	100	100	100	100	100	100	100	100	100
	2Ti/*	0.0836	0.1136	0.0814	0.0808	0.1247	0.0934	0.0866	0.0825	0.1168	0.1249	0.0854	0.0831	0.1185
	Cr/*	0.0015	0.0015	0.0014	0.0011	0.0017	0.0016	0.0022	0.0019	0.0015	0.0013	0.0012	0.0013	0.0012
Plotting	V/*	0.0026	0.0031	0.0030	0.0026	0.0037	0.0028	0.0034	0.0030	0.0035	0.0039	0.0031	0.0032	0.0037

Table 3 (continued). EMP analyses of titanohematite, cation formulae, end-member cal

	Traverse	1	1	1	5	5	5
	Point	34	36	37	1	13	16
	SiO2	*0.004*	*0.025*			*0.011*	*0.019*
	TiO2	5.012	4.43	4.117	4.726	5.484	4.303
	Al2O3	0.185	0.209	0.194	0.106	0.83	0.132
Wt%	Cr2O3	0.128	0.12	0.16	*0.055*	*0.051*	*0.077*
Oxides	V2O3	0.172	0.132	0.143	0.164	0.15	0.155
	a Nb2O5			*0.066*		*0.002*	
	a Ta2O5	*0.377*	*0.269*	*0.312*	*0.086*		
	Fe2O3	90.310	90.655	91.128	91.254	89.962	91.975
	Fe Tot (FeO)	84.519	83.964	85.067	85.178	83.387	85.55
	FeO	3.257	2.392	3.069	3.067	2.438	2.790
	MnO	*0.023*	*0.023*	*0.048*			*0.012*
	MgO	0.822	0.995	0.482	0.668	1.394	0.568
	CaO	*0.009*					*0.002*
	NiO				*0.05*	*0.025*	*0.078*
	Total	91.251	90.167	90.589	91.033	91.334	90.896
	Corr.Total	100.299	99.250	99.719	100.176	100.347	100.111
	Si	0.0001	0.0007	0.0000	0.0000	0.0003	0.0005
	Ti	0.0988	0.0881	0.0819	0.0933	0.1070	0.0851
	Al	0.0057	0.0065	0.0061	0.0033	0.0254	0.0041
Cats/2	Cr	0.0027	0.0025	0.0033	0.0011	0.0010	0.0016
	V3+	0.0036	0.0028	0.0030	0.0035	0.0031	0.0033
	Nb5+	0.0000	0.0000	0.0008	0.0000	0.0000	0.0000
	Ta5+	0.0027	0.0019	0.0022	0.0006	0.0000	0.0000
	Fe3+	1.7821	1.8048	1.8146	1.8036	1.7559	1.8199
	Fe Tot	1.8535	1.8577	1.8825	1.8710	1.8088	1.8812
	Fe2+	0.0714	0.0529	0.0679	0.0674	0.0529	0.0614
	Mg	0.0321	0.0392	0.0190	0.0262	0.0539	0.0223
	Mn	0.0005	0.0005	0.0011	0.0000	0.0000	0.0003
	Ca	0.0003	0.0000	0.0000	0.0000	0.0000	0.0001
	Ni	0.0000	0.0000	0.0000	0.0011	0.0005	0.0016
	Sum	2.0000	2.0000	2.0000	2.0000	2.0000	2.0000
	Sum Fe Tot	2.0000	2.0000	2.0000	2.0000	2.0000	2.0000
	Ox/2Cats	2.1090	2.0976	2.0927	2.0982	2.1221	2.0901
	3-Ox	0.8910	0.9024	0.9073	0.9018	0.8779	0.9099
	Fe3+	1.7821	1.8048	1.8146	1.8036	1.7559	1.8199
	Fe2+	0.0714	0.0529	0.0679	0.0674	0.0529	0.0614
	Fe3+/FeTot	0.9615	0.9715	0.9639	0.9640	0.9708	0.9674
	FeSiO3	0.0105	0.0661	0.0000	0.0000	0.0285	0.0500
	b FeNbO3	0.0000	0.0000	0.1184	0.0000	0.0035	0.0000
	c FeTaO3	0.4033	0.2903	0.3368	0.0921	0.0000	0.0000
	FeTiO3	6.5943	4.8384	6.1840	6.6138	5.2553	6.0851
End	MgTiO3	3.2128	3.9236	1.9011	2.6151	5.3892	2.2261
Members	MnTiO3	0.0511	0.0515	0.1076	0.0000	0.0000	0.0267
	CaTiO3	0.0253	0.0000	0.0000	0.0000	0.0000	0.0056
	NiTiO3	0.0000	0.0000	0.0000	0.1056	0.0522	0.1649
	Sum	10.2973	9.1699	8.6479	9.4267	10.7287	8.5585
	Fe2O3	89.1033	90.2387	90.7306	90.1794	87.7944	90.9935
	Cr2O3	0.1327	0.1255	0.1674	0.0571	0.0523	0.0800
	V2O3	0.1808	0.1400	0.1517	0.1727	0.1560	0.1634
	Al2O3	0.2859	0.3258	0.3025	0.1641	1.2686	0.2045
	Sum	89.7027	90.8301	91.3521	90.5733	89.2713	91.4415
	Total	100	100	100	100	100	100
	2Ti/*	0.1029	0.0911	0.0865	0.0943	0.1070	0.0851
	Cr/*	0.0013	0.0013	0.0017	0.0006	0.0005	0.0008
Plotting	V/*	0.0036	0.0028	0.0030	0.0035	0.0031	0.0033

Ratios	Al/*	0.0031	0.0029	0.0033	0.0038	0.0035	0.0029	0.0029	0.0026	0.0026	0.0026	0.0024	0.0036	Ratios	Al/*	0.0029	0.0033	0.0030	0.0016	0.0127	0.0020
	Mg/#	0.0175	0.0456	0.0170	0.0134	0.0679	0.0377	0.0222	0.0129	0.0628	0.0731	0.0282	0.0241	0.0664	Mg/#	0.0321	0.0392	0.0190	0.0261	0.0539	0.0223
	*=2Ti+R3+	2.0000	2.0000	2.0000	2.0000	2.0000	2.0000	1.9995	2.0000	2.0000	2.0000	1.9997	2.0000	1.9986	*=2Ti+R3+	1.9998	1.9987	2.0000	2.0000	1.9994	1.9990
	#=R2++(R3+/2	1.0008	1.0008	1.0012	1.0011	1.0007	1.0010	1.0023	1.0010	1.0015	1.0002	1.0015	1.0011	1.0012	#=R2++(R3+/2	1.0013	1.0010	1.0015	1.0003	1.0000	1.0000

Note: Wt% analyses in italics are below MDL (see Table 1A).
a Nb and Ta analyses, made due to presence of rutile, are suspect. Greater abundance of Ta than Nb is contrary to most occurences.
b 4/3 Fe2+ 2/3 Nb5+ O3
c 4/3 Fe2+ 2/3 Ta5+ O3

b 4/3 Fe2+ 2/3 Nb5+ O3
c 4/3 Fe2+ 2/3 Ta5+ O3

culations and plotting ratios.

5 20	5 21	Traverse Point	6 1	6 4	6 15
0.031	*0.014*	SiO2		*0.02*	*0.011*
4.648	4.162	TiO2	6.772	5.483	4.098
0.115	0.082	Al2O3	0.139	0.126	0.1
0.115	0.097	Cr2O3	0.08	0.1	0.101
0.159	0.113	V2O3	0.146	0.16	0.137
		a Nb2O5	*0.016*	*0.06*	*0.006*
0.035		Fe2O3	88.601	89.739	92.077
90.773	91.854	Fe Tot (FeO)	82.192	82.643	85.237
84.729	85.57	FeO	2.468	1.895	2.385
3.051	2.919	MnO			
	0.002	MgO	2.04	1.736	0.728
0.662	0.433	CaO			*0.002*
		NiO	*0.003*	*0.006*	
0.009	*0.069*	ZnO		*0.028*	*0.022*
90.503	90.542	Total	91.388	90.362	90.442
99.597	99.745	Corr.Total	100.265	99.353	99.667
0.0008	0.0004	Si	0.0000	0.0005	0.0003
0.0923	0.0827	Ti	0.1319	0.1081	0.0813
0.0036	0.0026	Al	0.0042	0.0039	0.0031
0.0024	0.0020	Cr	0.0016	0.0021	0.0021
0.0034	0.0024	V	0.0030	0.0034	0.0029
0.0000	0.0000	Nb5+	0.0002	0.0007	0.0001
0.0003	0.0000	Fe3+	1.7267	1.7712	1.8284
1.8037	1.8268	Fe Tot	1.7802	1.8127	1.8811
1.8710	1.8914	Fe2+	0.0535	0.0416	0.0526
0.0674	0.0645	Mg	0.0787	0.0679	0.0286
0.0261	0.0171	Mn			
0.0000	0.0000	Ca			0.0001
0.0000	0.0000	Ni	0.0001	0.0001	
0.0002	0.0015	Zn		0.0005	0.0004
2.0000	2.0000	Sum	2.0000	2.0000	2.0000
2.0000	2.0000	Sum FeTot	2.0000	2.0000	2.0000
		Ox/2Cats	2.1366	2.1144	2.0858
2.0982	2.0866	3-Ox	0.8634	0.8856	0.9142
0.9018	0.9134	Fe3+	1.7267	1.7712	1.8284
1.8037	1.8268	Fe2+	0.0535	0.0416	0.0526
0.0674	0.0645	Fe3+/FeTot	0.9700	0.9771	0.9720
0.9640	0.9659				
0.0819	0.0370	FeSiO3	0.0000	0.0525	0.0290
0.0000	0.0000	b FeNbO3	0.0281	0.1067	0.0107
0.0377	0.0000	FeTiO3	5.3081	3.9611	5.2204
6.6050	6.4153	MgTiO3	7.8749	6.7867	2.8634
2.6055	1.7058	MnTiO3			
0.0000	0.0045	CaTiO3			0.0057
0.0000	0.0000	ZnTiO3	0.0000	0.0542	0.0429
0.0191	0.1467	NiTiO3	0.0062	0.0127	0.0000
9.3491	8.3092	Sum	13.2173	10.9739	8.1721
90.1836	91.3420	Fe2O3	86.3370	88.5595	91.4221
0.1200	0.1013	Cr2O3	0.0819	0.1037	0.1054
0.1683	0.1197	V2O3	0.1516	0.1682	0.1449
0.1789	0.1277	Al2O3	0.2121	0.1947	0.1555
90.6509	91.6908	Sum	86.7827	89.0261	91.8279
100	100	Total	100	100	100
0.0927	0.0828	2Ti/*	0.1322	0.1092	0.0814
0.0012	0.0010	Cr/*	0.0008	0.0010	0.0011
0.0034	0.0024	V/*	0.0030	0.0034	0.0029

0.0018	0.0013	Al/*	0.0021	0.0019	0.0016
0.0261	0.0171	Mg/#	0.0787	0.0678	0.0286
1.9984	1.9993	*=2Ti+R3+	2.0000	2.0006	2.0007
1.0001	1.0000	#=R2++(R3+/2	1.0001	1.0004	1.0000

Table 3. TEM-EDX analyses, cation formulae, percentages of end members, and plotting ratios of titanohematite.

	Point	5	8	12	13	17	18	20	22
Feb. 6-8, 2007	O	60.00	60.01	60.00	60.00	60.00	60.00	60.00	60.00
	Ti	1.36	1.28	1.22	1.52	1.37	1.59	1.22	1.42
	Cr	0.03	0.05	0.02	0.04	0.05	0.03	0.03	0.04
Atom %	Mg	0.36	0.41	0.52	0.57	0.93	0.71	0.69	0.58
	Fe	38.25	38.26	38.24	37.87	37.65	37.66	38.05	37.97
	Total	100.00	100.01	100.00	100.00	100.00	99.99	99.99	100.01
	Ti	0.0680	0.0640	0.0610	0.0760	0.0685	0.0795	0.0610	0.0710
	Cr	0.0015	0.0025	0.0010	0.0020	0.0025	0.0015	0.0015	0.0020
	Fe3+	1.8625	1.8692	1.8770	1.8460	1.8605	1.8390	1.8760	1.8565
Cations/2	Mg	0.0180	0.0205	0.0260	0.0285	0.0465	0.0355	0.0345	0.0290
	(Fe Total)	1.9125	1.9127	1.9120	1.8935	1.8825	1.8830	1.9025	1.8985
	Fe2+	0.0500	0.0435	0.0350	0.0475	0.0220	0.0440	0.0265	0.0420
	(Total Cats)	2.0000	1.9997	2.0000	2.0000	2.0000	1.9995	1.9995	2.0005
	Total Cats	2.0000	1.9997	2.0000	2.0000	2.0000	1.9995	1.9995	2.0005
	Total Ox a	2.0688	2.0649	2.0615	2.0770	2.0698	2.0798	2.0613	2.0725
	TotalFe3+ b	1.8625	1.8692	1.8770	1.8460	1.8605	1.8390	1.8760	1.8565
	MgTiO3	1.8000	2.0497	2.6000	2.8500	4.6500	3.5500	3.4500	2.9000
Percentages of End Members	FeTiO3	5.0000	4.3493	3.5000	4.7500	2.2000	4.4000	2.6500	4.2000
	Sum	6.8000	6.3989	6.1000	7.6000	6.8500	7.9500	6.1000	7.1000
	Fe2O3	93.1250	93.4594	93.8500	92.3000	93.0250	91.9500	93.8000	92.8250
	Cr2O3	0.0750	0.1250	0.0500	0.1000	0.1250	0.0750	0.0750	0.1000
	Sum	93.2000	93.5844	93.9000	92.4000	93.1500	92.0250	93.8750	92.9250
	Total	100.0000	99.9833	100.0000	100.0000	100.0000	99.9750	99.9750	100.0250
Plotting Ratios	2Ti/*	0.0680	0.0640	0.0610	0.0760	0.0685	0.0795	0.0610	0.0710
	Cr/*	0.0008	0.0013	0.0005	0.0010	0.0013	0.0008	0.0008	0.0010
	Mg/#	0.0180	0.0205	0.0260	0.0285	0.0465	0.0355	0.0345	0.0290
	*=2Ti+R3+	2.0000	1.9997	2.0000	2.0000	2.0000	1.9995	1.9995	2.0005
	#=R2+R3/2	1.0000	0.9998	1.0000	1.0000	1.0000	0.9998	0.9998	1.0003
	Fe3+/FeTot	0.97386	0.97726	0.98169	0.97491	0.98831	0.97663	0.98607	0.97788

a = Total oxygen associated with each cation with Fe as FeO. b 2 (3-Total Ox)

Table 4. TEM-EDX analyses, cation formulae, percentages of end members, and plotting ratios of ferroan geikielite.

	Point	1	2	3	4	5	12	13	14	15	16	21	23
Feb.6-8, 2007	O	60.00	60.00	60.00	60.00	60.00	60.00	60.00	60.00	60.00	60.00	60.00	60.00
	Ti	19.04	19.48	19.77	20.13	20.96	19.36	19.53	21.27	20.72	20.05	20.48	20.73
	Cr	0.03	0.00	0.03	0.02	0.03	0.08	0.00	0.03	0.00	0.04	0.02	0.00
	Ni	0.03	0.00	0.00	0.01	0.03	0.00	0.04	0.02	0.01	0.04	0.02	0.00
Atom %	Mg	13.75	14.90	14.32	14.42	13.61	15.03	13.50	13.62	14.42	14.23	12.30	13.45
	Fe	7.15	5.55	5.84	5.35	5.35	5.50	6.91	5.07	4.83	5.62	7.15	5.79
	Mn	0.00	0.07	0.04	0.06	0.04	0.03	0.03	0.00	0.02	0.01	0.03	0.02
	Total	100.00	100.00	100.00	100.00	100.00	100.00	100.00	100.00	100.00	100.00	100.00	100.00
	Ti	0.952	0.974	0.989	1.007	1.048	0.968	0.977	1.064	1.036	1.003	1.024	1.037
Cations/2	Cr	0.002	0.000	0.002	0.001	0.002	0.004	0.000	0.002	0.000	0.002	0.001	0.000
	Ni	0.002	0.000	0.000	0.001	0.002	0.000	0.002	0.001	0.001	0.002	0.001	0.000
	Fe3+	0.095	0.052	0.022	-0.015	-0.096	0.060	0.047	-0.128	-0.072	-0.008	-0.049	-0.073
	Mg	0.688	0.745	0.716	0.721	0.681	0.752	0.675	0.681	0.721	0.712	0.615	0.673
	(Fe Total)	0.358	0.278	0.292	0.268	0.268	0.275	0.346	0.254	0.242	0.281	0.358	0.290
	Fe2+	0.263	0.225	0.270	0.282	0.364	0.215	0.298	0.382	0.314	0.289	0.407	0.363
	Mn	0.000	0.004	0.002	0.003	0.002	0.002	0.002	0.000	0.001	0.001	0.002	0.001
	(Total Cats)	2.000	2.000	2.000	2.000	2.001	2.000	2.001	2.001	2.000	2.000	2.000	2.000
	Total Cats	2.000	2.000	2.000	2.000	2.001	2.000	2.001	2.001	2.000	2.000	2.000	2.000
	Total Ox a	2.953	2.974	2.989	3.007	3.050	2.970	2.977	3.065	3.036	3.003	3.025	3.036
	Total Fe3+ b	0.095	0.052	0.022	-0.015	-0.096	0.060	0.047	-0.128	-0.072	-0.008	-0.049	-0.073
	NiTiO3	0.150	0.000	0.000	0.050	0.150	0.000	0.200	0.100	0.050	0.200	0.100	0.000
	MgTiO3	68.750	74.500	71.600	72.100	68.050	75.150	67.500	68.100	72.100	71.150	61.500	67.250
	FeTiO3	26.300	22.550	27.050	28.200	36.400	21.500	29.800	38.150	31.350	28.850	40.650	36.300
	MnTiO3	0.000	0.350	0.200	0.300	0.200	0.150	0.150	0.000	0.100	0.050	0.150	0.100
% of End Members	Sum	95.200	97.400	98.850	100.650	104.800	96.800	97.650	106.350	103.600	100.250	102.400	103.650
	Fe2O3	4.725	2.600	1.075	-0.725	-4.825	3.000	2.375	-6.400	-3.600	-0.375	-2.450	-3.675
	Cr2O3	0.075	0.000	0.075	0.050	0.075	0.200	0.000	0.075	0.000	0.100	0.050	0.000
	Sum	4.800	2.600	1.150	-0.675	-4.750	3.200	2.375	-6.325	-3.600	-0.275	-2.400	-3.675
	Total	100.000	100.000	100.000	99.975	100.050	100.000	100.025	100.025	100.000	99.975	100.000	99.975
Plotting Ratios	2Ti/*	0.952	0.974	0.989	1.007	1.047	0.968	0.976	1.063	1.036	1.003	1.024	1.037
	Cr/*	0.001	0.000	0.001	0.001	0.001	0.002	0.000	0.001	0.000	0.001	0.001	0.000
	Mg/#	0.688	0.745	0.716	0.721	0.680	0.752	0.675	0.681	0.721	0.712	0.615	0.673
	*=2Ti+R3+	2.000	2.000	2.000	2.000	2.001	2.000	2.001	2.001	2.000	2.000	2.000	2.000
	#=R2++(R3+/2)	1.000	1.000	1.000	1.000	1.001	1.000	1.000	1.000	1.000	1.000	1.000	1.000

a = Total oxygen associated with each cation with Fe as FeO. b 2 (3-Total Ox)

Table 5. EMP analyses, structural formulae, end members, and plotting ratios for retrograde vein hematite.

	Point	2	3	5	7	9	10	2
Wt% Oxides	SiO2		*0.004*	*0.004*			*0.017*	*0.011*
	TiO2			*0.028*		*0.002*	0.086	*0.04*
	Al2O3			*0.058*	*0.022*		*0.023*	*0.025*
	Cr2O3	*0.012*	*0.014*			*0.012*		*0.035*
	V2O3	0.052	*0.044*	0.137	0.054	0.075	0.116	0.256
	Fe Tot (FeO)	90.028	90.037	90.047	89.898	90.089	89.602	89.876
	MnO	*0.021*	*0.07*	*0.023*	*0.006*	*0.016*	*0.019*	
	MgO	*0.065*	*0.011*	*0.011*		*0.034*	*0.011*	
	CaO	*0.013*	*0.01*	*0.033*	*0.015*	*0.01*	*0.017*	
	ZnO					*0.11*		
	NiO			*0.011*	*0.042*	*0.003*	*0.016*	*0.008*
	Total	90.191	90.19	90.352	90.037	90.351	89.907	90.251
Cats/2	Si	0.0000	0.0001	0.0001	0.0000	0.0000	0.0005	0.0003
	Ti	0.0000	0.0000	0.0006	0.0000	0.0000	0.0017	0.0008
	Al	0.0000	0.0000	0.0018	0.0007	0.0000	0.0007	0.0008
	Cr	0.0003	0.0003	0.0000	0.0000	0.0003	0.0000	0.0007
	V	0.0011	0.0009	0.0029	0.0011	0.0016	0.0025	0.0054
	Fe3+	1.9986	1.9986	1.9940	1.9982	1.9981	1.9925	1.9909
	Mg	0.0026	0.0004	0.0004	0.0000	0.0013	0.0004	0.0000
	Zn	0.0000	0.0000	0.0000	0.0000	0.0021	0.0000	0.0000
	Fe2+	-0.0034	-0.0022	-0.0015	-0.0015	-0.0042	0.0005	0.0009
	Mn	0.0005	0.0016	0.0005	0.0001	0.0004	0.0004	0.0000
	Ca	0.0004	0.0003	0.0009	0.0004	0.0003	0.0005	0.0000
	Ni	0.0000	0.0000	0.0002	0.0009	0.0001	0.0003	0.0002
	Sum	2.0000	2.0000	2.0000	2.0000	2.0000	2.0000	2.0000
	Ox/2Cats	2.0007	2.0007	2.0030	2.0009	2.0010	2.0038	2.0046
	3-Ox	0.9993	0.9993	0.9970	0.9991	0.9990	0.9962	0.9954
	Fe3+	1.9986	1.9986	1.9940	1.9982	1.9981	1.9925	1.9909
	Fe2+	-0.0034	-0.0022	-0.0015	-0.0015	-0.0042	0.0005	0.0009
	Fe3+/FeTot	1.0017	1.0011	1.0007	1.0007	1.0021	0.9998	0.9995
	NiTiO3	0.0000	0.0000	0.0234	0.0897	0.0064	0.0342	0.0170
	FeSiO3	0.0000	0.0106	0.0106	0.0000	0.0000	0.0452	0.0291
	MgTiO3	0.2567	0.0435	0.0434	0.0000	0.1341	0.0436	0.0000
	ZnTiO3	0.0000	0.0000	0.0000	0.0000	0.2150	0.0000	0.0000
	FeTiO3	-0.3408	-0.2291	-0.1562	-0.1459	-0.4157	0.0029	0.0627

Percentages	MnTiO3	0.0471	0.1572	0.0515	0.0135	0.0359	0.0428	0.0000
of End	CaTiO3	0.0369	0.0284	0.0936	0.0427	0.0284	0.0484	0.0000
Members	Sum	0.0000	0.0106	0.0663	0.0000	0.0040	0.2172	0.1089
	Fe2O3	**99.9322**	**99.9280**	**99.6980**	**99.9081**	**99.9039**	**99.6231**	**99.5435**
	Cr2O3	0.0126	0.0147	0.0000	0.0000	0.0126	0.0000	0.0367
	V2O3	0.0552	0.0468	0.1453	0.0575	0.0796	0.1237	0.2720
	Al2O3	0.0000	0.0000	0.0904	0.0344	0.0000	0.0360	0.0390
	Sum	100.0000	99.9894	99.9337	100.0000	99.9960	99.7828	99.8911
	Total	100.0000	100.0000	100.0000	100.0000	100.0000	100.0000	100.0000
	2Ti/*	0.0000	0.0000	0.0006	0.0000	0.0000	0.0017	0.0008
Plotting	Cr/*	0.0001	0.0001	0.0000	0.0000	0.0001	0.0000	0.0004
Ratios	V/*	0.0011	0.0009	0.0029	0.0011	0.0016	0.0025	0.0054
	Al/*	0.0000	0.0000	0.0009	0.0003	0.0000	0.0004	0.0004
	Mg/#	0.0026	0.0004	0.0004	0.0000	0.0013	0.0004	0.0000
	*	2.0000	1.9998	1.9998	2.0000	2.0064	1.9991	1.9994
	#	1.0000	1.0000	1.0000	1.0000	1.0000	1.0000	1.0000

Note: Wt% analyses in italics are below MDL (see Table 1A).
* =2Ti+R3+ # =R2+ +(R3+/2)

Table 6. Lattice parameters and measured Néel temperatures of compositions close to X FeTiO3 = 0.84 and above.

	a (Å)	***c***(Å)	V(Å^3)	T_N
Synthetic end member (Wechsler and Prewitt 1984) X Ilm =1.00 X Hem = 0	5.0884	14.0855	315.84	57 K
Burton et al. 2008 Synthetic X Ilm = 0.974, X Hem = 0.026	5.0869	14.0667	315.23	43 K
Burton et al. 2008 Synthetic X Ilm = 0.915, X Hem 0.085	5.0843	14.0342	314.18	40 K
McEnroe et al. 2007b Allard Lake Quebec, AL36b X Ilm = 0.84, X Hem = 0.02, X Geik = 0.14	5.0828	14.0498	314.34	43 K
Robinson et al. 2006 Pramsknuten, Egersund, Norway X Ilm = 0.743 (incl. 0.005 $MnTiO_3$) X Hem = 0.045 (incl. 0.0015 Cr_2O_3, 0.0020 V_2O_3) X Geik = 0.212				~40 K 41.3 K[a]

[a] Brok et al. 2014 by single-crystal neutron diffraction.